

A hybrid approach combining DNS and RANS simulations to quantify uncertainties in turbulence modelling

Laurens J. A. Voet^{a,*}, Richard Ahlfeld^a, Audrey Gaymann^a, Sylvain Laizet^a, Francesco Montomoli^a

^a*Department of Aeronautics Imperial College London, Kensington, London, SW7 2AZ (UK)*

Abstract

Uncertainty quantification (UQ) has recently become an important part of the design process of countless engineering applications. However, up to now in computational fluid dynamics (CFD) the errors introduced by the turbulent viscosity models in Reynolds-Averaged Navier Stokes (RANS) models have often been neglected in UQ studies. Although Direct Numerical Simulations (DNS) are physically correct, obtaining a large enough set of DNS data for UQ studies is currently computationally intractable. UQ based only on RANS simulations or on DNS often leads to physical and statistical inaccuracies in the output probability distribution functions (PDF). Therefore, three hybrid methods combining both RANS simulations and DNS to perform non-intrusive UQ are suggested in this work. Low-fidelity RANS simulations and high-fidelity DNS are combined to give an approximation of an output PDF using the advantages of both data sets: the physical accuracy via the DNS and the statistical accuracy via the RANS simulations. The hybrid methods are applied to the flow over 2D periodically arranged hills. It is shown that the Gaussian CoKriging (GCK) method is the best hybrid method and that a non-intrusive hybrid UQ approach combining both DNS and RANS simulations is possible, with both physically more accurate and statistically better PDF.

Keywords: Uncertainty quantification, Non-intrusive hybrid methods, Gaussian CoKriging, Direct Numerical Simulation, Reynolds-Averaged Navier-Stokes simulation

1. Introduction

Uncertainty is one of the key points to consider in the design process or in the modelisation of physical systems. The uncertainty quantification process starts with a probability distribution function (PDF) of an input parameter, e.g. the freestream velocity over an airfoil. The PDF of an output parameter, e.g. the lift force of this airfoil, as a consequence of the uncertainty in the input parameter is of interest. Such uncertainties can have a large effect on the design and performance assessment for a wide variety of engineering applications, for example in turbine blade manufacturing (Thakur, Keane and Nair [1]), in structural properties such as stiffness and damping (Abolfathi et al. [2]), or in operating parameters such as fuel burn performance (Amaral et al. [3]).

*Corresponding author

Email address: laurens.voet@live.be (Laurens J. A. Voet)

Therefore, much research effort is put in developing methods to predict or quantify the effects of such uncertainties. In airfoil design, Loeven, Witteven and Bijl [4] showed for a NACA airfoil in transonic flow that manufacturing tolerances of maximum camber (in interval [3.5%, 6.5%] with mean $\mu = 5\%$), maximum camber location (in interval [29%, 51%] with mean $\mu = 40\%$) and maximum thickness (in interval [8.5%, 15.5%] with mean $\mu = 12\%$) can cause a 10% variation in shock location. In the field of turbomachinery, Schnell, Ashcroft and Hoehe [5] found that manufacturing errors effect compressor efficiency within $\pm 0.05\%$. In film cooling of gas turbine blades, Montomoli et al. [6] showed that heat transfer of the cooling holes can be affected by as much as 10% due to the manufacturing variation of filleted edges for a fillet radius to hole diameter ratio between 0 and 5 %. Panizza et al. [7] used it to confirm that a new series of centrifugal stage compressor blades was little affected by manufacturing uncertainty and therefore that the design was robust considering manufacturing variability. With the purpose of reducing the computational cost of the UQ process, Chan and Elsheikh [8] introduced a machine learning approach for efficient uncertainty quantification (UQ) using multi-scale methods, applied to elliptic problems.

The design process of such engineering applications is often governed by the use of very intricate and complex mechanical simulation models. In the field of fluids those models are Computational Fluid Dynamics (CFD) codes. The main interest in studying UQ using these models and in particular studying the propagation of input uncertainty is to obtain an accurate computation at low computational cost. However, since increasing accuracy generally leads to a considerable increase in computational cost, there is a demand for efficient numerical methods to perform UQ.

The simplest method to conduct UQ is by performing a Monte Carlo sampling on the response surface of a simulation model. As such the probability distribution of an output variable can be computed by presenting the results in a histogram. However, this approach can quickly become too computationally expensive, especially for high-fidelity computer simulations (Cunha Jr et al. [9]). In other words, running a very large number of high-fidelity simulations is computationally intractable and running fewer high-fidelity simulations would compensate the accuracy of the PDF. Another option to reduce the computational cost is to build a surrogate model of the response surface. This surrogate model is then sampled to get an approximation of the output probability distribution (O'Hagan [10]). Although this approach allows for more data points at a lower computational cost, such simulations are less accurate and therefore this approach would yield an less precise PDF. Since both above-mentioned approaches do not lead to accurate output PDF, different methods need to be developed to approximate the high-fidelity output PDF.

Specifically, an important distinction has to be made between different types of UQ methods, namely the difference between intrusive and non-intrusive UQ. In intrusive UQ, the computational model itself is adapted in different ways depending on the method before performing the uncertainty quantification analysis, e.g. in Köppel, Kröker and Rohde [11]. Non-intrusive UQ is used in this work, meaning that the computational model is used without any modification, but as a black box. The basic procedure of

a non-intrusive UQ method is as follows. The first step is to describe the design space uncertainties in a probabilistic framework. For example, model parameters are replaced with random variables (Loeven, Witteven and Bijl [4], Ahlfeld and Montomoli [12]), or a domain region is defined as a random field (Dow and Wang [13], Doostan, Geraci and Iaccarino [14]). In the second step, the model is run repeatedly for random samples drawn from the input probability distributions. Note that the computational model is run for all the samples and not adapted in any way to perform the UQ. The last step is to perform a statistical analysis using the results of the simulations to determine the probability distributions of the quantities of interest. A non-intrusive UQ method is valuable because in science or engineering applications computational models are available which can not be modified and can only be run for different input samples.

The previously depicted examples of uncertainty studies mostly fall under the field of the so-called aleatory UQ. The errors from such uncertainties are known, can be quantified using statistical methods, and can be studied for design exploration purposes. However, in addition to the field of aleatory UQ there is also the field of epistemic UQ. The term epistemic refers to uncertainties generated due to insufficient knowledge about the physical behaviour of a system. These kind of uncertainties have often been ignored in uncertainty studies.

In computer simulations of fluid dynamics multiple levels of fidelity exist. Argyropoulos and Markatos [15] highlight the recent advances (up to 2015) on the numerical modeling of turbulent flows specifically. Direct Numerical Simulations (DNS) are high-fidelity simulations and are considered as the true solution of a flow field. They are often used as a tool for turbulence model research, rather than a tool for design (Moin and Manesh [16]). The computational cost of DNS increases extremely rapidly with Reynolds number, which is a severe limitation for their application (Coleman and Sandberg [17]). On the other hand, Reynolds-Averaged Navier-Stokes (RANS) simulations using turbulent viscosity models to describe the Reynolds shear-stress term in the RANS equations are low-fidelity simulations, known to have errors when solving for a flow field. Using dimensional analysis, the turbulent viscosity depends on the product of a characteristic velocity and a characteristic length scale. This leads to several types of RANS simulations depending on how the turbulent viscosity is calculated, namely zero-equation or algebraic models (e.g. the mixing length hypothesis of Prandtl [18]), single-equation models (Spallart and Almaras [19]) and two-equation models (e.g. the $k-\omega$ model as formulated by Wilcox [20]). Another modelling approach for turbulent flows is Large Eddy Simulation (LES). Where the RANS simulations have closure models for the entire spectrum of turbulent scales, LES fully resolve the large scales while modelling the smaller sub-grid length scales (Sagaut [21]). It has to be noted that LES are not considered in this work. In the last few years, mainly due to recent progress in artificial intelligence (AI), lots of studies have been performed of RANS modelling making use of machine learning techniques. Duraisamy, Iaccarino and Xiao [22] recently reviewed the topic of turbulence modelling in the age of data. Wang, Wu and Xiao [23] and Wu, Xiao and Paterson [24] used a machine learning approach to reduce the uncertainties introduced by the RANS models. Machine learning also has been used as a tool to model the sub-grid

features in LES (Vollant, Balarac and Corre [25], Gamahara and Hattori [26]).

In the present work, the focus is on eddy viscosity models based on the Boussinesq hypothesis, like $k-\epsilon$ (Launder and Sharma [27]), $k-\omega$ (Wilcox [20]) and $k-\omega$ SST models (Menter, Kuntz and Langtry [28]). Approximating the effect of the Reynolds stresses on the mean flow field by prescribing a turbulent viscosity model generally works well for simple flows (Pope [29]). However, there are usually significant discrepancies for flows with strong adverse pressure gradients, flows close to separation, or flows where the streamline curvature is large (Wang, Wu and Xiao [30], Raiesi, Piomelli and Pollard [31]). The uncertainties in the flow introduced when using such RANS models are an example of the epistemic uncertainties mentioned above.

In recent years, the interest in UQ in the field of computational fluid mechanics has been increasing (Najm [32]). Knowing that significant errors exist in the RANS simulation models, UQ using purely RANS simulations leads to inaccurate results. Additionally, UQ using purely DNS is computationally intractable since running a large enough number of high-fidelity simulations for UQ is too expensive. Thus both methods have limitations in providing an accurate approximation of the output PDF. However, they also both have unique benefits that can be exploited when being combined. The high-fidelity DNS are computationally expensive but are very accurate. On the other hand, the low-fidelity RANS simulations are cheaper and therefore having access to a lot of data points allows for computations that are statistically more accurate. Noting that UQ involving DNS has never been attempted, the novelty of this work is the presentation of hybrid methods combining the data of both DNS and RANS simulations to perform an UQ study. The main objective of this work is to find methods in the field of fluid mechanics that combine all the pieces of information that are available from both RANS simulations and DNS, in an effective way that improves accuracy in computations within reasonable computational cost. The idea of hybrid or multi-fidelity modelling to perform UQ is also explored by Salehi et al. [33] on a transonic RAE2822 airfoil. Although multi-fidelity methods are studied, two sets of RANS simulations are used at two different mesh sizes as a low- and high-fidelity data set.

In this work three different hybrid methods for this hybrid framework are suggested. The methods are applied on the 2D channel flow over periodically arranged hills, an example test case often used in literature (Breuer et al. [34]) for reasons listed in Section 2.1. The Reynolds number, which is based on the bulk velocity through the channel and the hill height, is situated in the turbulent regime and equal to 5600. Geometric uncertainty is introduced in the shape of the hill by varying the hill steepness and the distance between subsequent hills. A set of output quantities of interest is selected for the UQ study, namely the height of the separation bubble at different streamwise locations and the streamwise length of the separation bubble. These quantities are related with the caveats associated with the RANS model, namely separation from a curved surface and reattachment. The propagation of the input uncertainty towards uncertainty in the output parameters is of interest. The output PDF generated with the different hybrid methods are compared using shape parameters (i.e. mean, standard deviation, range and skewness). For the purpose of this study the geometrical variations have been amplified to test the

hybrid methods; i.e. the variations are significantly larger than those to be encountered in the field of e.g. manufacturing tolerances. This amplification is applied to be able to better quantify the differences in these shape parameters.

2. Test Case, Numerical Modelling, Collocation Points, Quantities of Interest and CFD Validation

The flow over periodically arranged hills is chosen as a test case for the the hybrid UQ methods. The flow itself is studied extensively in literature, for example by Breuer et al. [34] or by Marquillie, Laval and Dolganov [35]. Wu, Xiao, and Paterson [24] used the flow over 2D periodically arranged hills as well as a test case for machine learning training. Gritskevich et al. [36] used the same test case for the development and validation of turbulence models. From existing literature it is therefore concluded that this flow case is well suited as a test case for the hybrid methods. The test case describes many important flow features such as separation from a curved surface and reattachment on a flat plate. The adverse pressure gradient due to the curved surface of the hill causes the flow to separate, creating a separation bubble behind the first hill. Further downstream the flow reattaches before it reaches the second hill. Also it is possible to compute the flow field at reasonable computational cost (Breuer et al. [34]). Since reliable experimental and numerical data of this flow is available by Breuer et al. [34], the exact same geometry is chosen to be able to validate the DNS model.

Since studying hybrid methods requires data of different levels of fidelity, high-fidelity DNS and low-fidelity RANS simulations of the flow over the hills are performed. In the following section, the reference test case is described as well as the numerical setup for both the DNS and RANS simulations. Next, the collocation points for applying the UQ methods, the quantities of interest and the CFD validation are delineated.

2.1. Test Case Description

The reference geometry of the test case is shown Figure 1. Variability in the hill geometry is introduced using two parameters, α and γ . The hill steepness angle parameter, α , scales the width of the hill and therefore its steepness as well. The hill streamwise separation parameter, γ , scales the separation between the two subsequent hills. The reference case ($\alpha = 1, \gamma = 1$) is the same as the Breuer test case. The flow over the periodically arranged hills is studied in the neighbourhood of the reference case by varying the hill geometry, namely by varying α and γ . The effect of changing α and γ is explained in more detail in Section 2.3.

The mathematical definition of the coordinates of the hill geometry (x_{hill}, y_{hill}) is described in Eq. 1-3 (Mellen, Fröhlich and Rodi [37]). The coordinates of the first hill are described by Eq. 1. The second hill is described by the same equation; the first hill is mirrored about the centre of the domain resulting

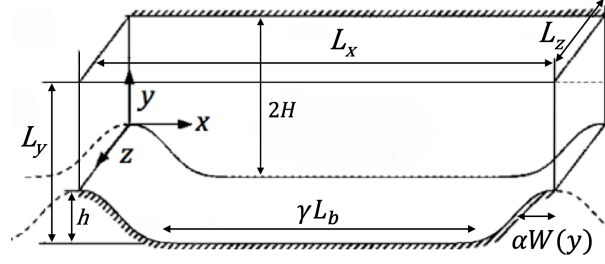


Figure 1: Definition of the test case: the 2D periodically arranged hills. The uncertainty input variables are the hill steepness angle (α) and the hill separation (γ).

in a symmetrical configuration.

$$\frac{y_{hill}(x_{hill})}{h} = \begin{cases} \min(1; 1 + 0 \cdot x_{hill} + 2.420 \cdot 10^{-4} \cdot x_{hill}^2 - 7.588 \cdot 10^{-5} \cdot x_{hill}^3), & x_{hill}|_1 \in [0, 0.3214h] \\ 0.8955 + 3.484 \cdot 10^{-2} \cdot x_{hill} - 3.629 \cdot 10^{-3} \cdot x_{hill}^2 + 6.749 \cdot 10^{-5} \cdot x_{hill}^3, & x_{hill}|_2 \in [0.3215h, 0.5h] \\ 0.9213 + 2.931 \cdot 10^{-2} \cdot x_{hill} - 3.234 \cdot 10^{-3} \cdot x_{hill}^2 + 5.809 \cdot 10^{-5} \cdot x_{hill}^3, & x_{hill}|_3 \in [0.5h, 0.7143h] \\ 1.445 - 4.927 \cdot 10^{-2} \cdot x_{hill} + 6.950 \cdot 10^{-4} \cdot x_{hill}^2 - 7.394 \cdot 10^{-6} \cdot x_{hill}^3, & x_{hill}|_4 \in [0.7144h, 1.071h] \\ 0.6401 + 3.123 \cdot 10^{-2} \cdot x_{hill} - 1.988 \cdot 10^{-3} \cdot x_{hill}^2 + 2.242 \cdot 10^{-5} \cdot x_{hill}^3, & x_{hill}|_5 \in [1.071h, 1.429h] \\ \max(0; 2.0139 - 7.180 \cdot 10^{-2} \cdot x_{hill} + 5.875 \cdot 10^{-4} \cdot x_{hill}^2 + 9.553 \cdot 10^{-7} \cdot x_{hill}^3), & x_{hill}|_6 \in [1.429h, 1.929h] \end{cases} \quad (1)$$

The mathematical definition of how the parameters α and γ modify the hill geometry is given in Eq. 2. When ($\alpha = 1, \gamma = 1$), the total length $\frac{L}{h} = 9$, which is the Breuer test case.

$$\frac{L}{h} = 3.858\alpha + 5.142\gamma \quad (2)$$

The parameter α varies the width of the hill by stretching the x-coordinates of each of the 6 sections of the geometry, as given in Eq. 3 below. Therefore, the hill height becomes:

$$\frac{y_{hill}}{h} = \frac{y_{hill}(x'_{hill})}{h} \quad \text{where} \quad x_{hill}' = [x_{hill}|_1, x_{hill}|_2, x_{hill}|_3, x_{hill}|_4, x_{hill}|_5, x_{hill}|_6] \cdot \alpha \quad (3)$$

The first and second hill are connected by a flat floor in the middle such that the total length of the domain satisfies Eq. 2.

It is important to understand why this test case is relevant for evaluating the newly suggested hybrid UQ methods. First of all, as stated before, the test case is often studied in literature. Secondly, although the flow over periodically arranged hills is very simple, CFD methods based on solving the RANS equations still struggle with calculating the flow field accurately. More specifically, they mainly have problems with predicting the length and the height of the separation bubble. This means that the epistemic uncertainties stemming from the RANS model are visible when studying the flow around the

reference case ($\alpha = 1, \gamma = 1$). Thirdly, the shape of the curved surface, more specifically the steepness of the hill, strongly affects the reattachment position. The steepness of the hill can be related to the diverging angle in diffusers, which mainly determines the flow pattern in through it (Huminić and Gabriela [38]). Therefore, variations in the hill geometry will cause uncertainty in output flow variables because of uncertainty in the RANS closure model and thus varying the hill steepness and hill separation is an effective way of introducing uncertainty in the flow test case.

2.2. Numerical modelling of the flow field

The low-fidelity RANS simulations and high-fidelity DNS simulations, are performed at a Reynolds number (Re) of 5600, which is based on the bulk velocity through the channel (U_b) and the hill height (h). The choice for this Reynolds number is firstly based on the availability of experimental and numerical data to validate the models. Secondly, with the practical motivation of keeping the computational cost of the DNS simulations reasonably low to collect a relevant amount of DNS points to set up a hybrid framework. RANS simulations have been performed at similar Reynolds numbers, i.e. around $Re \approx 5600$ (Choi, V.T. Nguyen and J. Nguyen [39]), and even as low as 2800 for the same flow as in the present study (Xiao et al. [40]). At such Reynolds numbers, the range of turbulent scales is large enough for a RANS approach to be relevant while a DNS approach is still manageable in terms of computational resources. Similar flow features would still be expected at higher Reynolds numbers, namely a recirculation bubble downstream of the hill separation point. The bulk velocity through the channel is calculated based on the definition of the Reynolds number, namely $U_b = \mu_{air} Re / (h \rho_{air}) = 2.9714 \text{ m/s}$ where the air density $\rho_{air} = 1.225 \text{ kg/m}^3$ and dynamic viscosity $\mu_{air} = 1.82 \cdot 10^{-5} \text{ Pa} \cdot \text{s}$. As characteristic length the hill height $h = 0.028 \text{ m}$ is used, as given in Almeida, Duraó and Heitor [41]. Both the high-fidelity DNS and the low-fidelity RANS simulations are discussed in Section 2.2.1 and Section 2.2.2 respectively. The 3D unsteady DNS results are averaged over the span-wise direction and over a time period to generate the mean 2D flow field. The RANS simulations are performed by directly using a 2D flow option.

2.2.1. Immersed boundary method Direct Numerical Simulation setup and validation with reference data

The DNS are performed on a computational domain with size $L_x \times L_y \times L_z = 9.000h \times 3.036h \times 4.500h$, with h being the hill height. The coordinate system is orthonormal, with coordinate x in the stream-wise direction, y in the vertical direction and z in the span-wise direction, as depicted in Figure 1. A Cartesian mesh with $512 \times 257 \times 128$ mesh nodes in the respective directions is employed. A stretched mesh in the y -direction is used, which is slightly refined near the walls. The spatial resolution is as good as the ones found in previous numerical studies for the same Reynolds number. More information about the DNS grid can be found in Breuer et. al [34]. As boundary conditions, a periodic interface is used in both the stream-wise and span-wise directions; a non-slip condition is used both at the top and bottom wall of the channel. The initial condition for the streamwise velocity field $u(y)$ as a function of the y -direction is a parabolic Poiseuille profile given by Eq. 4, where H is the semi-channel height and

U_0 is the center-line velocity. Note that Eq. 4 is applied at the section of the channel in between the hills using the origin at the semi-channel height.

$$u(y) = U_0 \left(1 - \left(\frac{y}{H} \right)^2 \right) \quad (4)$$

The following method is used to start the simulations. First, they are launched without any hill geometry up to the point when a fully developed flow is obtained. The periodic boundary conditions in stream-wise direction require a dynamically adjusted pressure gradient at each time step in order to maintain a constant mass flow rate through the channel, i.e. the pressure gradient is adjusted implicitly by the use of a forcing term in the Navier-Stokes equations (Quadrio, Frohnapfel and Hasegawa [42]). The forcing term changes at every time step in such a way that the resultant flow rate is equal to a prescribed flow rate, as given by Eq. 5. Note that the DNS are performed using normalised variables, namely $U_0 = 1$, $\rho_{air} = 1$ and $H = 1$. The reference massflow rate per unit span is non-dimensionalised as well and is computed from the Poiseuille profile, as given in Eq. 5. The massflow rate is kept constant for all DNS.

$$\dot{m} = \frac{1}{2H} \left(\rho_{air} U_0 \int_{-H}^H 1 - \left(\frac{y}{H} \right)^2 dy \right) = \frac{2\rho_{air} U_0}{3} \quad \leftrightarrow \quad \dot{m} = \frac{2}{3} \quad (5)$$

After obtaining a fully developed channel flow, the hill geometry is introduced into the computational domain. Note that the data are collected only after a transitional period, from the point when the flow is fully developed again. A simulation time step $\Delta t = 0.0005H/U_b$ is used. For all the calculations, turbulent statistical data have been collected over a time period $T = 150H/U_b$.

The DNS are performed using the Incompact3d high-order flow solver (Laizet and Lamballais [43] and Laizet and Li [44]). More details about the DNS data set of the flow over periodic hills can be found in Xiao et al. [45]. The hill geometry is modeled using a customised immersed boundary method based on a direct forcing approach. A direct forcing approach adds a forcing function to the incompressible Navier-Stokes equations. The forcing function is zero in the fluid domain but non-zero inside the body, i.e. the hill geometry. By adding such a forcing function the zero-velocity boundary condition at the wall of the hill is satisfied. The Incompact3d code is based on sixth-order compact schemes for the spatial discretisation on the Cartesian mesh and a third-order Adams-Bashforth scheme for the time advancement. Note that the convective terms of the incompressible Navier-Stokes equations are written in skew-symmetric form. This reduces aliasing errors while remaining energy conserving for the type of spatial discretisation considered here. To treat the incompressibility condition, a fractional step method is used to solve a Poisson equation. For efficiency reasons, this equation is solved in spectral space using appropriate 3D Fast-Fourier Transforms (FFT). In order to have a strict equivalence between the finite-difference operators in physical space and the spectral operators, the concept of modified wave

number is used, introduced by Lele [46]. This reduces the accuracy of the spectral operators to sixth-order accuracy. Note that the divergence free condition, i.e. the incompressible continuity equation, is ensured up to machine accuracy. Finally, the pressure mesh is staggered from the velocity mesh by half a mesh-element to avoid spurious pressure oscillations. More details about the code, especially about the original treatment of the pressure in spectral space, can be found in Laizet and Lamballais [43]. Because of the size of the simulations, the parallel version of Incompact3d has been used for this numerical work. Based on a highly scalable 2D decomposition library and a distributed FFT interface, it is possible to use it on thousands of computational cores. More details about this efficient parallel strategy can be found in Laizet and Li [44].

The immersed boundary method DNS model is validated using the numerical and experimental data, given by Breuer et al. [34]. The reference data is available in the European Research Community On Flow, Turbulence And Combustion (Ercoftac) database¹. The profiles of both the horizontal velocity and the turbulent kinetic energy at different span-wise locations are compared to the reference data of Breuer. The comparison can be seen in Figure 2.

When comparing the horizontal velocity profiles in Figure 2, it can be seen that the immersed boundary method DNS model is able to match the reference data. Especially the separation and reattachment features are accurately described by the model. This makes the immersed boundary method DNS model trustworthy for this study. The mismatch between the experimental and numerical turbulent kinetic energy profiles in Figure 2 should be noted. However, both the numerical data of Breuer et al. [34] and the immersed boundary method DNS model deviate from the experimental data in the region between the hills, which indicates that the numerical data is consistent. Moreover, the immersed boundary method DNS turbulent kinetic energy profiles are in between the experimental results and the reference DNS of Breuer. As an example at $x/h = 2$, the maximum difference between Breuer experimental and DNS data is 10.4%, while the maximum difference between the experimental results and the immersed boundary method DNS is only 6.3%. From this comparison it can be concluded that the immersed boundary method DNS model is well suited as a high-fidelity model to describe the test case of the flow over 2D periodically arranged hills.

2.2.2. Reynolds-Averaged Navier-Stokes Simulation setup and grid convergence study

The 2D RANS simulations are performed using Siemens Star-CCM+ software. The computational domain, shown in Figure 2.2.1, is two-dimensionalised meaning the domain with size $L_x \times L_y = 9h \times 3.036h$ remains. A two-dimensional mesh is constructed using an ‘Automatic 2D Mesh’ after applying the ‘Badge for 2D Meshing’ operation in Star-CCM+². A polygonal mesh with non-dimensional base size $\frac{b_{mesh}}{h} = 0.036$ is selected based on a mesh independence study, which is illustrated in Figure 3.

¹The Ercoftac data base can be accessed through this link: http://www.kbwiki.ercoftac.org/w/index.php/UFR_3-30_Test_Case

²More information on 2D meshing in Star-CCM+ can be found here: <http://mdx2.plm.automation.siemens.com/ko/node/7426>

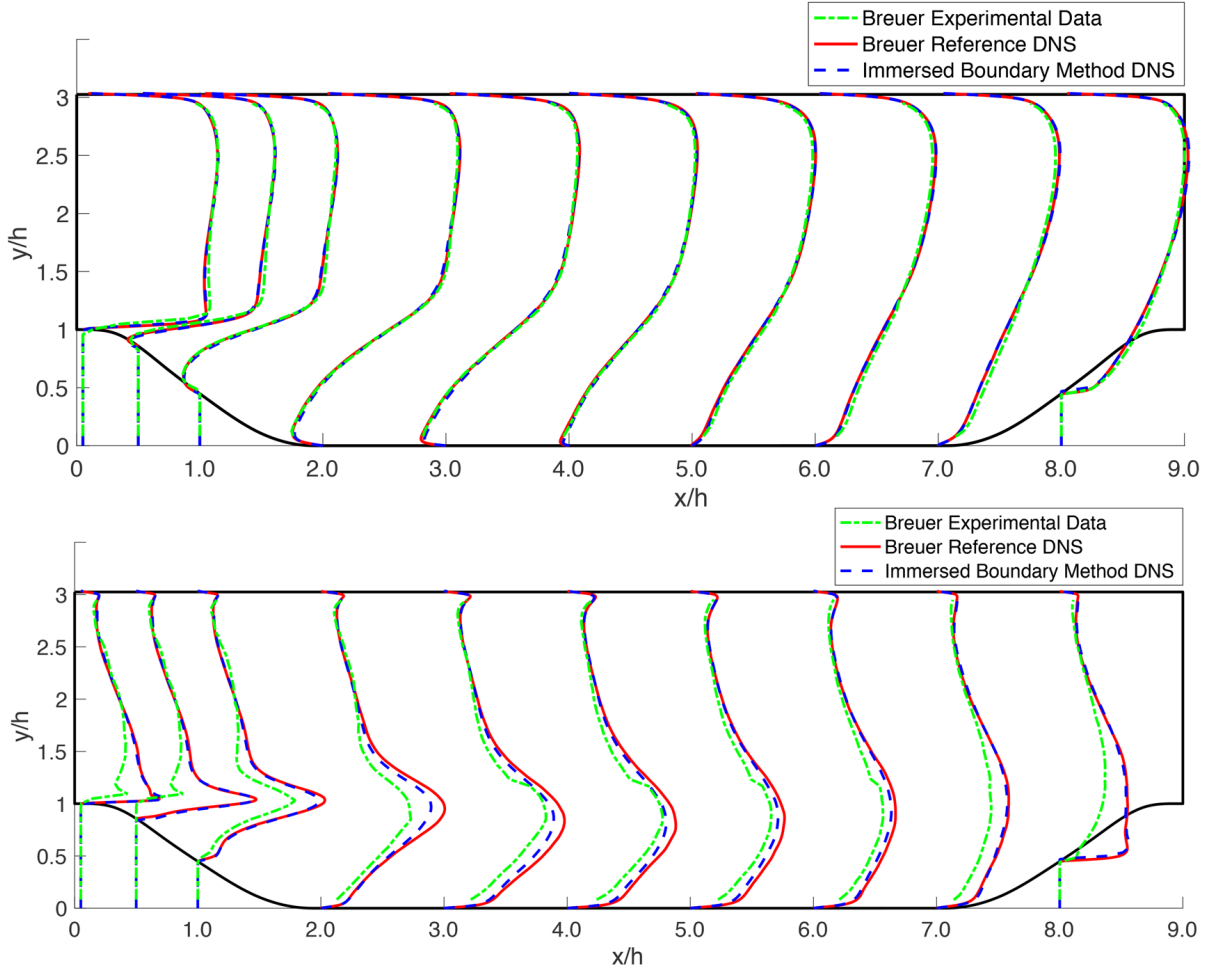


Figure 2: Validation of the immersed boundary method DNS model of the reference case ($\alpha = 1$, $\gamma = 1$) by comparing horizontal velocity profiles (top) and turbulent kinetic energy (bottom) profiles with experimental and numerical data.

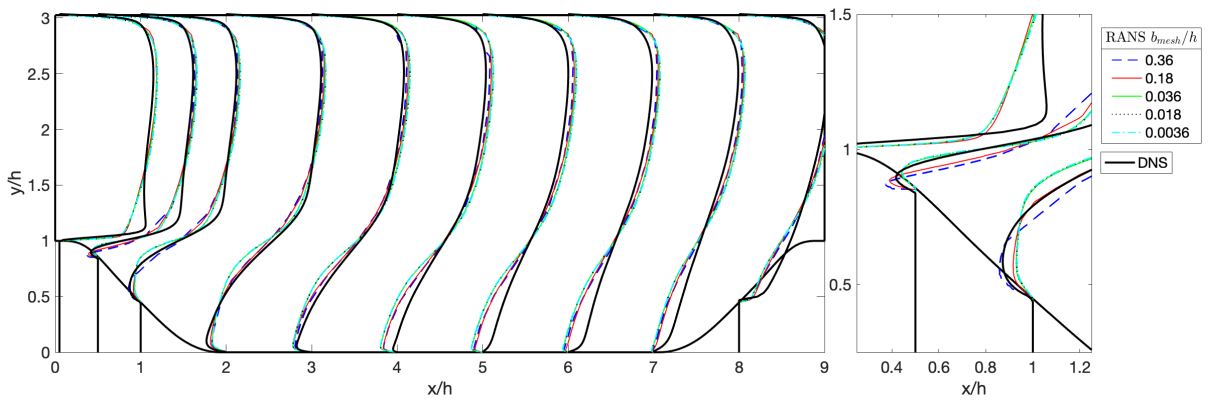


Figure 3: Grid convergence study for RANS ($k - \omega$ SST) reference case ($\alpha = 1$, $\gamma = 1$) for the entire fluid domain (left) and for position $x/h = 1$ (right). Different non-dimensional base sizes of the RANS (0.36 to 0.0036) simulations are compared with the DNS results.

This study is performed to be able to select the largest possible mesh size resulting in accurate data which does not significantly vary from a very fine mesh. This reduces the computational cost of the

simulations. The reference test case ($\alpha = 1, \gamma = 1$) is run with non-dimensional base sizes varying from 0.36 to 0.0036. From Figure 3, it can be seen that the results are converged at a non-dimensional base size of 0.036. The convergence can also be seen by looking at the quantities of interest, as described in Section 2.4. In Table 1 the bubble height at $x/h = 2$ and $x/h = 4$ is shown as a function of the mesh size.

Table 1: Grid convergence study for the bubble height at streamwise locations $x/h = 2$ and $x/h = 4$ for the RANS ($k - \omega$ SST) reference case ($\alpha = 1, \gamma = 1$).

Quantity of Interest \ Mesh base size	0.36	0.18	0.036	0.018	0.0036
Bubble height at $x/h = 2$	0.54	0.56	0.62	0.625	0.625
Bubble height at $x/h = 4$	0.4	0.41	0.47	0.475	0.475

A base mesh size of 0.036 results in 41800 mesh cells for the reference test case ($\alpha = 1, \gamma = 1$). As boundary conditions, a non-slip condition has been selected for the upper and lower wall of the domain. For the inlet and outlet of the fluid domain, periodic boundary conditions have been selected with a fully-developed interface. The average driving pressure gradient for the reference test case ($\alpha = 1, \gamma = 1$) in the RANS simulation is $\frac{dp}{dx} = -3.45 Pa/m$.

To resolve the boundary layer of the hill 40 prism layers are applied with a prism layer stretching of 1.2. For the reference test case this results in wall y^+ values between 1 and 1.025. The incompressible RANS equations are solved using a turbulent, gas and segregated flow option. To select an appropriate turbulence model for the test case, the horizontal velocity profiles of Star-CCM+ $k - \epsilon$, $k - \omega$ SST, Spalart-Allmaras models and the immersed boundary method DNS are compared. This comparison can be seen in Figure 4. The $k - \omega$ Shear Stress Transport (SST) turbulence model is chosen because of its suitability for separated flows (Menter, Kuntz and Langtry[28]). A periodic translational interface with fully developed flow option is selected between the inlet and outlet of the channel. As for the DNS, the horizontal velocity profile in the channel is initialised using a Poiseuille flow condition. Each of the RANS simulations is run for 10000 iterations. This results in residuals below $4 \cdot 10^{-10}$ for the continuity, U and V momentum, turbulent kinetic energy and turbulent dissipation rate equation when evaluated for the reference test case ($\alpha = 1, \gamma = 1$).

2.3. Collocation points for UQ study

At a fixed Reynolds number, the two main parameters that influence the flow over the periodically arranged hills are the steepness and the successive spacing of the hills. Hence, two parameters are introduced to control the uncertainty of the geometry, namely α and γ as defined in Figure 1 and Eq. 2. The reference test case is defined by ($\alpha = 1, \gamma = 1$). The parameter α changes the hill steepness. Physically, this changes the adverse pressure gradient the flow experiences when flowing down the hill. Therefore it is expected to influence the separation point. The parameter γ varies the spacing in between subsequent hills and is therefore expected to influence the reattachment point. It also has to be noted that the magnitude of the geometric variations in the test case is significantly larger than what would be expected for e.g. machining uncertainty. In this case the variation in the geometry is amplified to

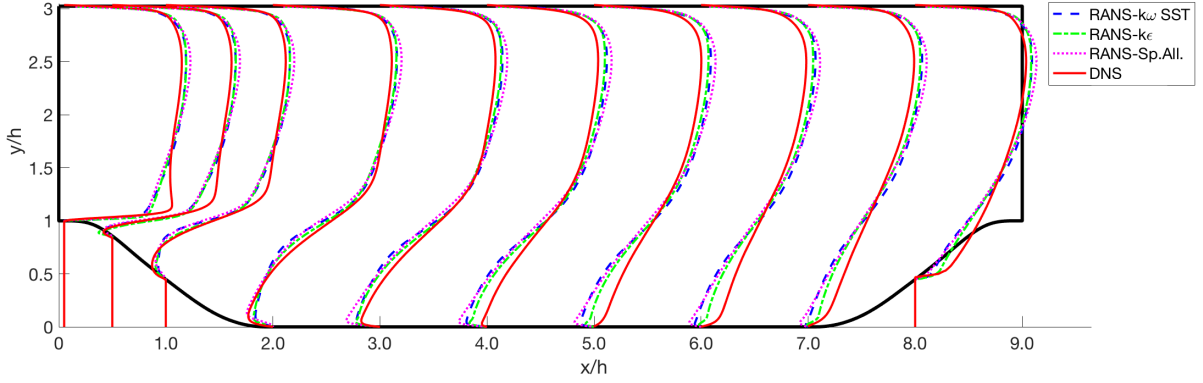


Figure 4: Comparison of horizontal velocity profiles of Star-CCM+ $k - \epsilon$, $k - \omega$ SST, Spalart-Allmaras turbulence models and the immersed boundary method DNS for the reference case ($\alpha = 1$, $\gamma = 1$).

determine if the methods are working. Note that engineering or scientific problems often have a lot more than 2 varying parameters. The methods which are proposed in Section 3 apply to such problems as well as to the test case which is described in this work. However, here only two parameters are selected for simplicity.

It is assumed that a set of data points around the reference case for both DNS and RANS are given and that this set cannot be modified. This is a situation which can be encountered in reality; for example a set of simulations is available and there is no time nor money to run a new set. For this example the number of DNS data points $N_{DNS} = 7$ and the number of RANS data points $N_{RANS} = 30$. The two sets of collocation points are illustrated in Figure 5 as well as the corresponding geometric variation of the hills for the DNS collocation points.

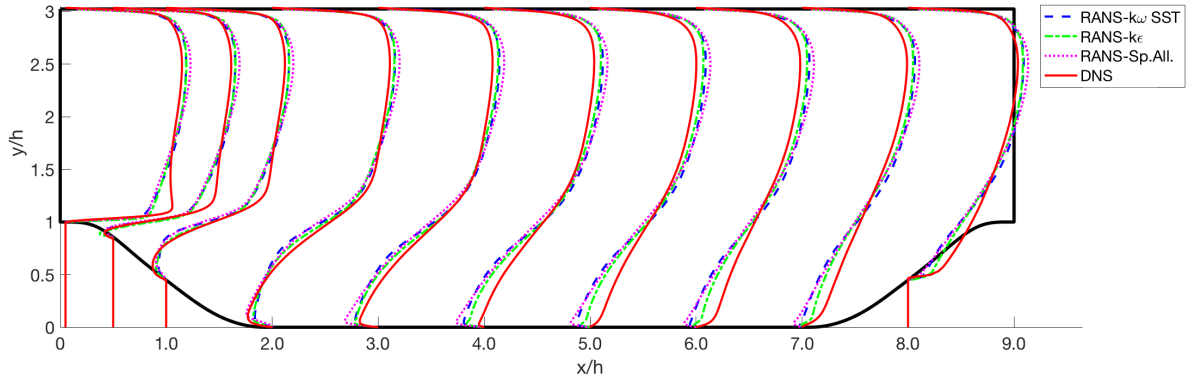


Figure 5: Collocation points of the DNS (x) and RANS simulations (o) (left). DNS grid points with geometrical variation of α , γ (right).

Some remarks have to be made regarding the available data set. First of all, note that the two sets of collocation points are nested meaning that the DNS points are a subset of the RANS points. Secondly, the DNS collocation points are located in a T-shape such that no high-fidelity information is present in the bottom left and bottom right corner of the $(\alpha - \gamma)$ domain. In these regions, the low-fidelity RANS

collocation points are expected to assist significantly in determining the shape of the hybrid response surface. This shows that the construction of the set of high- and low-fidelity collocation points in this test case already indicates a useful application of the hybrid methods. Furthermore, it has to be noted that the number of data points used in this study is relatively low compared to other studies; e.g. Garzon and Darmofal [47] used 150 blade surface measurements in their probabilistic approach to quantify the impact of geometric variability on compressor aerodynamic performance. However, since high-fidelity data is computationally very expensive, such a situation can easily be encountered in an engineering framework. The idea of the numerical methods that are proposed in Section 3 is exactly the same for a small or a larger data set. For the purpose of this study a smaller number of simulations is chosen to decrease the numerical cost. To conclude it is important to mention that the numerical methods are not restricted for a specific number of simulations or a specific arrangement of collocation points. Finally, this work focuses on presenting hybrid methods for uncertainty quantification using both high-fidelity and low-fidelity data. It does not focus on the physical understanding of the flow over the periodically arranged hills, e.g. the consequences of varying parameters α and γ .

2.4. Output Quantities of Interest

The hybrid UQ study is applied on a set of Quantities of Interest (QoI). The QoI are selected based on the weaknesses of the RANS model, namely parameters describing separation and reattachment:

1. The height of the separation bubble (y_{bubble}/h) at streamwise position $x/h = 2$. This streamwise position is chosen because the flow is expected to be fully separated at $x/h = 2$ for all collocation points.
2. The height of the separation bubble (y_{bubble}/h) at streamwise position $x/h = 4$. This streamwise position is chosen because the reattachment point of the DNS is expected to be at approximately $x/h = 4$.
3. The streamwise length of the separation bubble (x_{bubble}/h).

The height of the separation bubble at the different streamwise locations is calculated using the following criterion: the region in the y -direction with a negative x -component of velocity is defined as the separation bubble. Physically, the separation bubble height represents losses in the flow. Its presence acts as an equivalent geometry for the flow through the channel.

The streamwise length of the separation bubble is calculated using a criterion related to the skin-friction coefficient along the hill geometry. The distance in between the points where the skin-friction coefficient falls below a threshold $C_f < 10^{-3}$ is selected as the length of the separation bubble. This is illustrated in Figure 6 for the DNS reference case ($\alpha = 1$, $\gamma = 1$). Note that a smoothing filter is applied on the skin-friction coefficient signal for illustrative purposes.

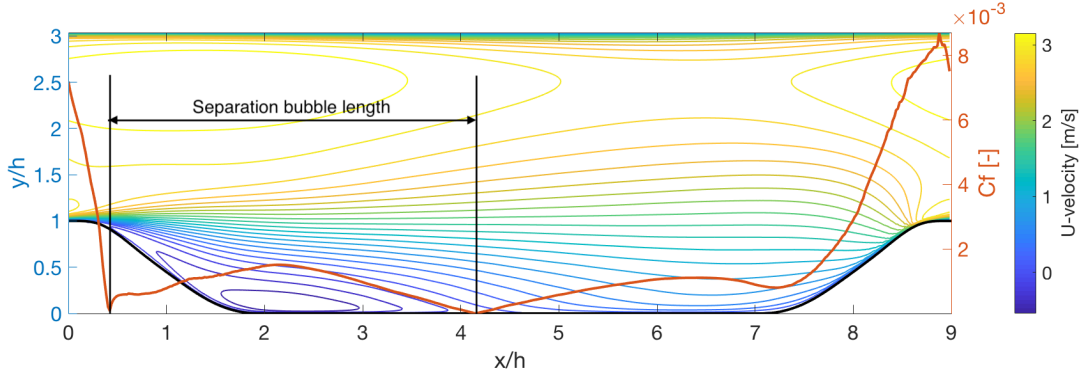


Figure 6: Horizontal velocity contours and skin-friction coefficient (C_f) along the hill wall for the DNS reference test case ($\alpha = 1, \gamma = 1$).

3. Hybrid Uncertainty Quantification Methods

Two sets of simulations of the flow over periodically arranged hills are now available. As shown in Figure 5, a set of $N_{DNS} = 7$ high-fidelity DNS and a set of $N_{RANS} = 30$ low-fidelity RANS simulations are given. With all this data available, the purpose of this study is to describe the flow over the hills around the reference case ($\alpha = 1, \gamma = 1$) as accurately as possible. It has to be noted that both data sets model the same physical phenomenon. Therefore, the information of both data sets can be combined to be able to give a better description of the flow rather than using one of the individual data sets. The hybrid methods delineated in this section allow to combine all this information that is available. It has to be noted that the hybrid methods are applicable to any test case in which a hybrid data set is available. Therefore, the mathematics of the methods are delineated as generally as possible. The application of the methods to the problem of the flow over the periodically arranged hills in particular is depicted in Section 5.1.

Since the data of the simulations are only available at discrete collocation points, the hybrid methods need to have the ability to interpolate between results. In other words, the methods create a response surface using the data points. The response surface can be evaluated, at or in between the available data points. Moreover, the hybrid methods are often derived from general interpolation methods for a single data set. The interpolation is performed in the space of the random variables that are used to introduce uncertainty in the geometry, i.e. in this work the $(\alpha - \gamma)$ -space. These methods have to be adapted to be applied to a hybrid data set. Three such methods are described in this section to generate a hybrid response surface. For every method, the general interpolation method is described first. Secondly, the hybrid method is described. The three methods that are set out are the Inverse Weighted Distance (IWD) method, the Polynomial Chaos Expansion using Regression (PCER) method and the Gaussian CoKriging method (GCK).

Finally, the hybrid response surfaces are used to sample the output PDF to quantify the uncertainty on one of the QoI as a result of the geometric input uncertainty. Section 3.4 describes the method to compute the PDF for the IWD method and the GCK method. The PCER hybrid method directly results

in a PDF, meaning that for this method Section 3.4 is not applicable.

3.1. Inverse Weighted Distance (IWD) method

The IWD method results in a response surface $f_{IWD}(\boldsymbol{\xi})$, where $\boldsymbol{\xi} = [\xi_1, \xi_2, \dots, \xi_n]$ is a multivariate variable dependent on n input variables. In the following sections, $\boldsymbol{\xi} = [\alpha, \gamma]$. The response surface is sampled according to a specific input probability distribution function to generate the probability distribution function of the output QoI.

3.1.1. General IWD method

The IWD method is a simple method developed by Shepard [48] for interpolation of irregularly-spaced data of function f . The method is given in Eq. 6 and Eq.7 for a data set of N data points. For points $\boldsymbol{\xi}_i$ where data is available, the response surface is equal to the function value of the data point itself, namely $f(\boldsymbol{\xi}_i)$. For all other points $\boldsymbol{\xi}$, the hybrid response surface $f_{IWD}(\boldsymbol{\xi})$ is generated by a weighted average of given datapoints $\boldsymbol{\xi}_i$ with function values $f(\boldsymbol{\xi}_i)$.

$$f_{IWD}(\boldsymbol{\xi}) = \begin{cases} \frac{\sum_{i=1}^N w_i(\boldsymbol{\xi}, \boldsymbol{\xi}_i) f_i(\boldsymbol{\xi}_i)}{\sum_{i=1}^N w_i(\boldsymbol{\xi}, \boldsymbol{\xi}_i)} & \text{if } d(\boldsymbol{\xi}, \boldsymbol{\xi}_i) \neq 0 \text{ for all } i \\ f_i(\boldsymbol{\xi}_i) & \text{if } d(\boldsymbol{\xi}, \boldsymbol{\xi}_i) = 0 \text{ for some } i \end{cases} \quad (6)$$

$$w_i(\boldsymbol{\xi}, \boldsymbol{\xi}_i) = \frac{1}{d(\boldsymbol{\xi}, \boldsymbol{\xi}_i)^p} \quad (7)$$

The weights in the IWD method are a power p of the inverse distance between the data point $\boldsymbol{\xi}_i$ and the point where the response surface is evaluated $\boldsymbol{\xi}$. Note that in Eq. 6-7 the function $d(\boldsymbol{\xi}, \boldsymbol{\xi}_i)$ denotes the distance between points $\boldsymbol{\xi}$ and $\boldsymbol{\xi}_i$. For the simplest IWD method, $p = 1$, such that the weights are literally the inverse distance between $\boldsymbol{\xi}_i$ and $\boldsymbol{\xi}$. Other values for the power p are also possible.

3.1.2. Hybrid IWD method

The general IWD method is adapted to be used in a hybrid framework in which a low-fidelity and high-fidelity data set are available. This is given in Eq. 8 for a set of N_{lf} low-fidelity and N_{hf} high-fidelity data points. For the IWD model, the function value of the high-fidelity data $f_{hf}(\boldsymbol{\xi}_i)$ is used for points where this data is available. For points where only low-fidelity data is available, the general IWD method is applied to the difference between high and low-fidelity data points (i.e. $f_{hf}(\boldsymbol{\xi}_i) - f_{lf}(\boldsymbol{\xi}_i)$) to compute the addition to the low-fidelity data $f_{lf}(\boldsymbol{\xi})$. The weights are based on distance as can be seen in Eq. 7. Note that in its form Eq. 8 can only be used to compute $f_{IWD}(\boldsymbol{\xi})$ at the low-fidelity data points. This form of the equation is used to explain the concept of hybrid IWD; the equation can easily be adapted to predict data in between low-fidelity data points as well.

$$f_{IWW}(\boldsymbol{\xi}) = \begin{cases} f_{lf}(\boldsymbol{\xi}) + \frac{\sum_{i=1}^{N_{hf}} w_i(\boldsymbol{\xi}, \boldsymbol{\xi}_i) (f_{hf}(\boldsymbol{\xi}_i) - f_{lf}(\boldsymbol{\xi}_i))}{\sum_{i=1}^{N_{hf}} w_i(\boldsymbol{\xi}, \boldsymbol{\xi}_i)} & \text{if } d(\boldsymbol{\xi}, \boldsymbol{\xi}_i) \neq 0 \text{ for all } i \\ f_{hf}(\boldsymbol{\xi}_i) & \text{if } d(\boldsymbol{\xi}, \boldsymbol{\xi}_i) = 0 \text{ for some } i \end{cases} \quad (8)$$

3.2. Polynomial Chaos Expansion using Regression (PCER) method

The main idea of polynomial chaos is to build an expansion of a stochastic output function f_{PCER} using a polynomial basis and a set of coefficients (Ahlfeld, Belkouchi and Montomoli [49]). The output probability distribution function is generated directly instead of first generating a hybrid response surface, which is sampled afterwards. Different methods exist to calculate the coefficients of the polynomial chaos expansion (PCE), namely a point collocation method or a spectral projection method (Palar, Tsuchiya and Parks [50]). In this section, the point collocation method is described, in which the coefficients are calculated using a weighted regression approach.

3.2.1. General PCER method

Polynomial Chaos is a method used to approximate a stochastic output model $f(\boldsymbol{\xi})$ dependent on n independent stochastic input random variables, namely $\boldsymbol{\xi} = [\xi_1, \xi_2, \dots, \xi_n]$. The input random variables have event spaces $\Omega_1, \Omega_2, \dots, \Omega_n$ and probability distribution functions (PDFs) $\rho_1, \rho_2, \dots, \rho_n$. The stochastic model output is expanded into a linear combination of multivariate orthogonal polynomials Ψ_k with coefficients c_k .

$$f(\boldsymbol{\xi}) = \sum_{k=1}^{\infty} c_k \Psi_k(\boldsymbol{\xi}) \approx \sum_{k=1}^{N_p} c_k \Psi_k(\boldsymbol{\xi}) \quad (9)$$

The number of linear combination terms N_p for a polynomial expansion of order m is usually truncated to $N_p = \frac{(n+m)!}{n!m!}$. The multivariate orthogonal polynomials Ψ_k are calculated as the product of univariate orthogonal polynomials $\psi_{I_k^i}^i$:

$$\Psi_k(\boldsymbol{\xi}) = \prod_{i=1}^d \psi_{I_k^i}^i(\xi_i) \quad \text{where } k \in 1, 2 \dots N_p \quad (10)$$

To achieve exponential convergence, the basis functions $\psi_{I_k^i}^i$ used in Eq. 10 are chosen to be orthogonal polynomials corresponding to the PDF ρ_i of the input random variable ξ_i (Loeven, Witteven and Bijl [4]). The definition of a polynomial orthogonal with respect to a probability distribution is based on the inner product and is given in Eq. 11, where δ_{ij} is the Kronecker delta (Palar, Tsuchiya and Parks [50]). Two examples of orthogonal polynomials are the Hermite and Legendre functions, which are corresponding to the normal and uniform probability distribution respectively (Hosder and Walters [51]). The orthogonal polynomials of different order are computed using a recurrence relation.

$$\langle \Psi_i(\boldsymbol{\xi}), \Psi_j(\boldsymbol{\xi}) \rangle = \int_{\Omega} \Psi_i(\boldsymbol{\xi}) \Psi_j(\boldsymbol{\xi}) \rho(\boldsymbol{\xi}) d\boldsymbol{\xi} = \delta_{ij} \quad (11)$$

The order of univariate orthogonal polynomial $\psi_{I_k^i}^i$ in Eq. 10 that contributes to the multivariate orthogonal polynomial Ψ_k is stored in the multi-index matrix elements I_k^i , having dimensions $N_p \times n$. Note that the multi-index matrix of n random variables for a PCE of order m $I_{n,m}$ contains the elements I_k^i (where $k \in [1, n]$ and $i \in N_p$). The rows of the matrix represent the different combinations of how the

degree of the polynomial chaos expansion m can be divided over the number of variables n . The following simple example for $n = 2$ random variables and a degree of polynomial chaos expansion $m = 2$ shows how this matrix can be interpreted. The number of terms in the expansion is equal to $N_p = \frac{(2+2)!}{2!2!} = 6$.

$$I_6^2 = \left[\begin{array}{cccccc} [0, 0], & [1, 0] & [0, 1] & [2, 0] & [1, 1] & [0, 2] \end{array} \right]^T \quad (12)$$

The coefficients c_k in Eq. 9 of the polynomial chaos expansion can be computed in different ways. In this section, a least-squares regression approach is chosen. Another approach could be to use nested optimal Gaussian sparse grids and apply Gaussian quadrature to obtain the coefficients (Ahlfeld, Belkouchi and Montomoli [49]). To compute the coefficients using the regression approach, a set of N_{eval} arbitrary samples $\boldsymbol{\eta} = [\eta_1, \eta_2 \dots \eta_{N_{eval}}]$ is taken for which the stochastic output model f is evaluated. The number of evaluations N_{eval} is equal to the number of simulations; for the low-fidelity data $N_{eval} = N_{lf}$, for the high-fidelity data $N_{eval} = N_{hf}$. These samples are inserted in Eq. 9. The coefficients c_k are found by solving the linear system of equations, given in Eq. 13. This approach is also called point-collocation non-intrusive Polynomial Chaos and was successfully applied by Loeven, Witteven and Bijl [4] to investigate geometric airfoil uncertainty.

$$\begin{array}{c} [\Psi] \\ \left[\begin{array}{ccc} \Psi_1(\eta_1) & \cdots & \Psi_{N_p}(\eta_1) \\ \vdots & \ddots & \vdots \\ \Psi_1(\eta_{N_{eval}}) & & \Psi_{N_p}(\eta_{N_{eval}}) \end{array} \right] \end{array} \begin{array}{c} [c] \\ \left[\begin{array}{c} c_1 \\ \vdots \\ c_{N_p} \end{array} \right] \end{array} = \begin{array}{c} [F] \\ \left[\begin{array}{c} f(\eta_1) \\ \vdots \\ f(\eta_{N_{eval}}) \end{array} \right] \end{array} \quad (13)$$

The regression approach requires the number of evaluations N_{eval} to be larger or equal than the number of coefficients N_p to compute. An over-sampling ratio $N_{eval}/N_p = 2$ is advised by Palar, Tsuchiya and Parks [50] and Hosder, Walters and Balch [52] to reduce the matrix condition number and the likelihood of overfitting. The least-squares solution c of the system is given by Eq. 14.

$$c = (\Psi^T \Psi)^{-1} \Psi^T F \quad (14)$$

Instead of solving the linear regression problem directly, the problem can also be transformed in a weighted least-squares problem. The weighted least-squares solution gives the coefficients c for the polynomial chaos expansion. The expression for c is given in Eq. 15.

$$c = (\Psi^T \lambda \Psi)^{-1} \Psi^T \lambda F \quad (15)$$

The method to generate the weight matrix λ in Eq. 15, is illustrated in Figure 7. First a linear least-square regression is generated to predict the trend of the DNS (*Right figure, mesh 1*). Subsequently, this trend is translated to the mean of the RANS simulations (*Right figure, mesh 2*). This results in a plane,

which is denoted by κ . The inverse distance $1/d(\kappa, \xi_i)$ of each RANS data point ξ_i to the translated plane is chosen as the weight factor.

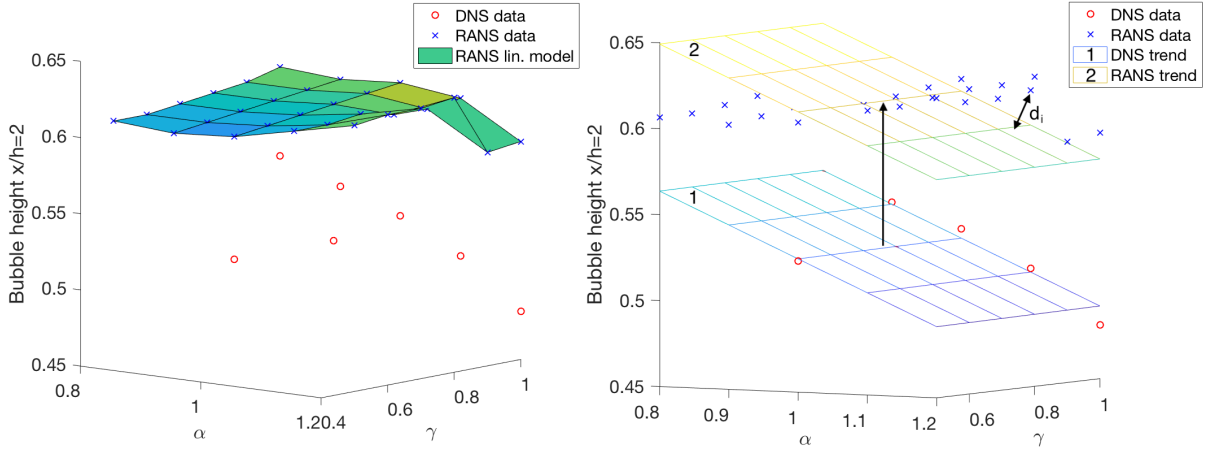


Figure 7: Illustration of the method to determine the weight factors for weighted least-squares regression. RANS linearly interpolated response surface (left). DNS trend shifted to the mean value of RANS points (right). The distance of RANS point x_i to the shifted trend is indicated as d_i .

The reasoning for this modification of the method introduced by Palar, Tsuchiya and Parks [50] is that this weighting mechanism assigns higher priority to the low-fidelity model data points if they capture the trend of the high-fidelity model well and a lower weight if they fail to capture the trend of the high-fidelity data points.

3.2.2. Hybrid PCER method

Where the general PCER method works on a single data set, the hybrid PCER model is constructed using two data sets. A low-fidelity data set is used to generate a low-fidelity PCE (i.e. $P_{m,n}$ in Eq. 16). This PCE is improved by using a correction PCE (i.e. $P_{m-r,n}$ in Eq. 16) using both the high and low-fidelity data set. This is given in Eq. 16. The operator $P_{m,n}$ is a low-fidelity PCE of n variables with an expansion order equal to m . Since less high-fidelity data points are available compared to low-fidelity data points, the order of the correction PCE will be lower than the order of the low-fidelity PCE (i.e. the value of r in Eq. 16 depends on how many high-fidelity data points are available and is used to indicate that the order of the correction PCE is lower than the order of the low-fidelity PCE).

$$f_{PCER}(\xi) = P_{m,n}[f_{lf}(\xi)] + P_{m-r,n}[C(\xi)] \quad (16)$$

The correction function C can be either an additive or multiplicative function of the low and high-fidelity data points, as given in Eq. 17 or a combination of both (Ng and Eldred [53]). Note that in Eq. 16 an additive correction function is applied.

$$C_{additive}(\xi) = f_{hf}(\xi) - f_{lf}(\xi), \quad C_{multiplicative}(\xi) = \frac{f_{hf}(\xi)}{f_{lf}(\xi)} \quad (17)$$

The PCE operators of the low-fidelity model and the correction model are given in Eq. 18 and Eq. 19 respectively. The low-fidelity coefficients $c_{lf,i}$ and the correction coefficients $c_{C,i}$ are determined in the same way as the general PCER method using only the low-fidelity data set and both data sets respectively.

$$P_{m,n}[f_{lf}(\boldsymbol{\xi})] = \sum_{i \in I_{m,n}} c_{lf,i} \Psi_i(\boldsymbol{\xi}) \quad (18)$$

$$P_{m-r,n}[C(\boldsymbol{\xi})] = \sum_{i \in I_{m-r,n}} c_{C,i} \Psi_i(\boldsymbol{\xi}) \quad (19)$$

In this way, Eq. 16 is reformulated using both a low-fidelity and a correction PCE. The result is given in Eq. 20. In this methodology only the lower-order expansion coefficients are corrected by high-fidelity data. The higher-order coefficients of the expansion are calculated from the low-fidelity model only.

$$f_{PCER}(\boldsymbol{\xi}) = \sum_{i \in I_{m,n} \setminus I_{m-r,n}} c_{lf,i} \Psi_i(\boldsymbol{\xi}) + \sum_{i \in I_{m-r,n}} (c_{lf,i} + c_{C,i}) \Psi_i(\boldsymbol{\xi}) \quad (20)$$

3.3. Gaussian CoKriging (GCK) method

The Kriging method, developed by D. G. Krige [54] in the field of geostatistics, is a general interpolation method, applied to a single data set. The CoKriging method makes use of the ordinary Kriging method and applies it to two data sets with different levels of fidelity, a low- and a high-fidelity data set. A brief overview of both the Kriging and CoKriging method are given in Section 3.3.1 and Section 3.3.2 respectively.

3.3.1. Kriging

Whereas the IWD method only uses distance as a weight factor, the Kriging method also uses correlation and regression in the interpolation process. The method is applied to a data set of N data points $\boldsymbol{\xi}_i$, where each data point depends on a set of n input variables (i.e. $\boldsymbol{\xi} = [\xi_1, \xi_2 \dots \xi_n]$). To predict the function value in a new point $\boldsymbol{\xi}_{N+1}$, the set of N data points is used as given in Eq. 21. Note that the function value $f_{Krig}(\boldsymbol{\xi}_{N+1})$ is called the Kriging predictor. The Kriging surrogate model is constructed by approximating the stochastic output model $f_{Krig}(\boldsymbol{\xi}_{N+1})$ by separating the model response in a mean global trend μ and a local term Z , a stationary Gaussian process representing the fluctuations from this mean trend (Forrester, Sobester and Keane [55]).

$$f_{Krig}(\boldsymbol{\xi}_{N+1}) = \mu + Z(\boldsymbol{\xi}_{N+1}, \boldsymbol{\xi}_i) \quad \forall i \in [1, N] \quad (21)$$

Note that since $Z(\boldsymbol{\xi})$ indicates the fluctuation from the mean trend μ , the expectation $E[Z(\boldsymbol{\xi})] = 0$ and the covariance $cov[Z(\boldsymbol{\xi}), Z(\boldsymbol{\xi}_i)] = \sigma^2 \psi(\boldsymbol{\xi}, \boldsymbol{\xi}_i)$. The fluctuating term $Z(\boldsymbol{\xi})$ is approximated by an expansion of basis functions, namely $Z(\boldsymbol{\xi}) = \sum_{i=1}^N b_i \Psi_i$. The function Ψ_i denotes the multi-variate correlation function

between the point where the Kriging predictor is evaluated and the data points $\boldsymbol{\xi}_i$. The general multivariate correlation function is the product of n individual univariate correlation functions, as given in Eq. 22.

$$\Psi(\boldsymbol{\xi}, \boldsymbol{\xi}_i) = \prod_{k=1}^n \psi(\xi^k, \xi_i^k) \quad (22)$$

The correlation function describes the relationship between the data points in the domain (e.g. linear, Gaussian, exponential correlation function, etc.). The choice of which correlation function to use is governed by the underlying physical phenomenon which is modelled (Lophaven, Nielsen and Søndergaard [56]). As an example the exponential correlation function is given in Eq. 23.

$$\psi(\xi^k, \xi_i^k) = \exp(-\theta_k |\xi^k - \xi_i^k|) \quad (23)$$

By looking at Eq. 22 and Eq. 23, it can be seen that the multivariate correlation function depends on a set of n hyper-parameters θ_k . Substituting everything back into Eq. 21, the value of the Kriging predictor $f_{Krig}(\boldsymbol{\xi}_{N+1})$ is found by performing a maximum likelihood estimate (MLE) of the hyper-parameters θ_k and the mean trend μ . The MLE of the variable is indicated by $(\hat{\cdot})$, e.g. the MLE of μ is indicated with $\hat{\mu}$.

$$f_{Krig}(\boldsymbol{\xi}_{N+1}) = \hat{\mu} + \sum_{i=1}^N b_i \Psi_i(\boldsymbol{\xi}_{N+1}, \boldsymbol{\xi}_i) \quad (24)$$

The constants of the expansion in Eq. 24 are given by $\mathbf{b} = \Psi^{-1}(\mathbf{f} - \mathbf{1}\hat{\mu})$. Ψ denotes an $n \times n$ matrix storing the correlations of the data set, \mathbf{f} is an $n \times 1$ matrix storing the function values of the data points and $\mathbf{1}$ is a $n \times 1$ unit vector. More information on the Kriging method can be found in Forrester, Sobester and Keane [55].

3.3.2. CoKriging

As described in the previous section, the Kriging method builds an approximation of the output model from a single data set. The CoKriging process uses two data sets to approximate an output response function, namely a cheap or low-fidelity data set and an expensive or high-fidelity data set. The low- and high-fidelity data is concatenated in one hybrid matrix, as given in Eq. 25. The independent variables of the data points are concatenated in matrix \mathbf{X} and the dependent variables are concatenated in matrix \mathbf{Y} .

$$\mathbf{X} = \begin{bmatrix} \mathbf{X}_{lf} \\ \mathbf{X}_{hf} \end{bmatrix} \quad \text{and} \quad \mathbf{Y} = \begin{bmatrix} \mathbf{Y}_{lf} \\ \mathbf{Y}_{hf} \end{bmatrix} \quad (25)$$

It is assumed that $\text{cov}(Y_{hf}(\boldsymbol{\xi}^i), Y_{lf}(\boldsymbol{\xi}) | Y_{lf}(\boldsymbol{\xi}^i)) = 0 \quad \forall \boldsymbol{\xi} \neq \boldsymbol{\xi}^i$. This means that in the points where high-fidelity data is available, this data is assumed to be equal to the true value regardless of the low-fidelity data. Just like in the Kriging model, the output model is approximated by the sum of a mean

trend and a Gaussian process. In this case, the CoKriging predictor is denoted by $f_{CoKrig}(\boldsymbol{\xi}_{N+1})$ and the high-fidelity Gaussian process Z_{hf} consists of a scaled low-fidelity Gaussian process Z_{lf} and a difference Gaussian process Z_δ , as given in Eq. 26.

$$Z_{hf}(\boldsymbol{\xi}) = \rho Z_{lf}(\boldsymbol{\xi}) + Z_\delta(\boldsymbol{\xi}) \quad (26)$$

The parameter Z_δ in Eq. 26 refers to the difference between the high-fidelity data and scaled low-fidelity data evaluated at the high-fidelity data points (the scaling factor is ρ). Note that this requires the low- and high-fidelity set of collocation points to be nested.

Whereas Kriging has a covariance matrix, the CoKriging method has a matrix \mathbf{C} composed of several covariance matrices. Eq. 27 is given without a derivation; the detailed construction of the matrix \mathbf{C} can be found in Forrester, Sobester and Keane [55].

$$\mathbf{C} = \begin{pmatrix} \sigma_{lf}^2 \Psi_{lf}(\mathbf{X}_{lf}, \mathbf{X}_{lf}) & \rho \sigma_{lf}^2 \Psi_{lf}(\mathbf{X}_{lf}, \mathbf{X}_{hf}) \\ \rho \sigma_{lf}^2 \Psi_{lf}(\mathbf{X}_{hf}, \mathbf{X}_{lf}) & \rho^2 \sigma_{lf}^2 \Psi_{lf}(\mathbf{X}_{hf}, \mathbf{X}_{hf}) + \sigma_d^2 \Psi_d(\mathbf{X}_{hf}, \mathbf{X}_{hf}) \end{pmatrix} \quad (27)$$

Finally, the value of the CoKriging predictor $f_{CoKrig}(\boldsymbol{\xi}_{N+1})$ is found by performing a MLE on the hyper-parameters in the covariance matrix (i.e. $\hat{\theta}_k$), the mean (i.e. $\hat{\mu}$), the standard deviations (i.e. $\hat{\sigma}_c$ and $\hat{\sigma}_d$) and the scaling factor (i.e. $\hat{\rho}$). This is given in Eq. 28. The variable \mathbf{c} in Eq. 28 is given by Eq. 29.

$$f_{CoKrig}(\boldsymbol{\xi}_{N+1}) = \hat{\mu} + \mathbf{c}^T \mathbf{C}^{-1} (\mathbf{Y} - \mathbf{1}\hat{\mu}) \quad (28)$$

$$\mathbf{c} = \begin{bmatrix} \hat{\rho} \hat{\sigma}_{lf}^2 \psi_{lf}(\mathbf{X}_{lf}, \boldsymbol{\xi}_{N+1}) \\ \hat{\rho} \hat{\sigma}_{lf}^2 \psi_{lf}(\mathbf{X}_{hf}, \boldsymbol{\xi}_{N+1}) + \hat{\sigma}_d^2 \psi_d(\mathbf{X}_{hf}, \boldsymbol{\xi}_{N+1}) \end{bmatrix} \quad (29)$$

More information on the CoKriging method can be found in Forrester, Sobester and Keane [55].

3.4. Generation of output PDF

In general, the PDF describing the uncertainty of an output variable as a consequence of uncertainty of an input variable is generated by running a large number of model simulations (i.e. a Monte Carlo sampling) and subsequently by generating a histogram of the output values.

However, in this work the available data set only contains a small number of data points, namely N_{lf} and N_{hf} . Running a large set of simulations is generally computationally too expensive, especially for the high-fidelity model. Therefore the output model is sampled in only a few data points (namely $N_{lf} = 30$ and $N_{hf} = 7$) and subsequently these data points are linearly interpolated in $\boldsymbol{\xi}$ -space to form a response surface (i.e. a surrogate model). It has to be noted that the methods above are applicable for any generic problem and the most appropriate type of interpolation is dependent on the physics problem. In this work, not knowing the physics of the problem beforehand, linear interpolation is chosen for simplicity. A Monte Carlo simulation of the response surfaces is performed using 10^5 samples to generate the PDF.

Similar number of Monte Carlo function evaluations are used by Klaus and Eichstädt [57] in a Monte-Carlo based uncertainty propagation study with hierarchical models and by Bartel, Stoudt and Possolo [58]. The output of the Monte Carlo simulation is visualised in a normalised histogram.

The PDFs of the interpolated low- and high-fidelity surrogate model are generated by only using the data points that are available from the simulations. Since the IWD-method and the GCK method also result in a hybrid output model, they are also evaluated in the grid points of the low-fidelity model. These evaluations are also linearly interpolated and the Monte Carlo sampling is also applied to this response surface to generate the hybrid PDF of the output variable. Finally, the PCER-method is designed to directly results in a PDF.

4. DNS and RANS results

4.1. Comparison of the contours of streamwise velocity

The horizontal velocity contours for both the DNS and RANS simulations of the reference test case ($\alpha = 1, \gamma = 1$) are shown in graphs (1a) and (1b) of Figure 8. The DNS and RANS simulations for the case ($\alpha = 0.8, \gamma = 1$) are shown in graphs (2a) and (2b). One of the main differences between the DNS and the RANS $k - \omega$ SST results is the location of the reattachment point. For the reference test case ($\alpha = 1, \gamma = 1$), the reattachment point for the DNS is at $x/h = 4.148$ and for the RANS simulation at $x/h = 7.684$, a difference of 85%.

For the test case ($\alpha = 0.8, \gamma = 1.0$), the DNS reattachment location is $x/h = 4.769$, unlike for the RANS simulations, it is $x/h = 7.291$. Therefore it is expected that the QoI described in Section 2.4, i.e. the length of the circulation bubble and the height of the separation bubble at different streamwise locations will be significantly different for the DNS and RANS $k - \omega$ SST results.

It is concluded that significant differences can be seen in the results of the RANS model compared to the DNS. Doing UQ using the RANS results alone will therefore result in inaccurate outcomes. This issue can be resolved by using both RANS simulations and DNS in a hybrid framework for UQ, which is the purpose of this work.

4.2. Comparison of the quantities of interest

The results for the quantities of interest for both the DNS and RANS simulations are summarized in Table 2 for the reference test case ($\alpha = 1, \gamma = 1$).

Table 2: Comparison of the quantities of interest for the DNS and RANS simulations of the reference test case ($\alpha = 1, \gamma = 1$). Note that all the quantities of interest are non-dimensionalised with the hill height h .

Quantity of Interest	DNS	RANS
Height of the bubble at $x/h = 2$	0.53	0.62
Height of the bubble at $x/h = 4$	0.14	0.47
Bubble length	3.73	7.45

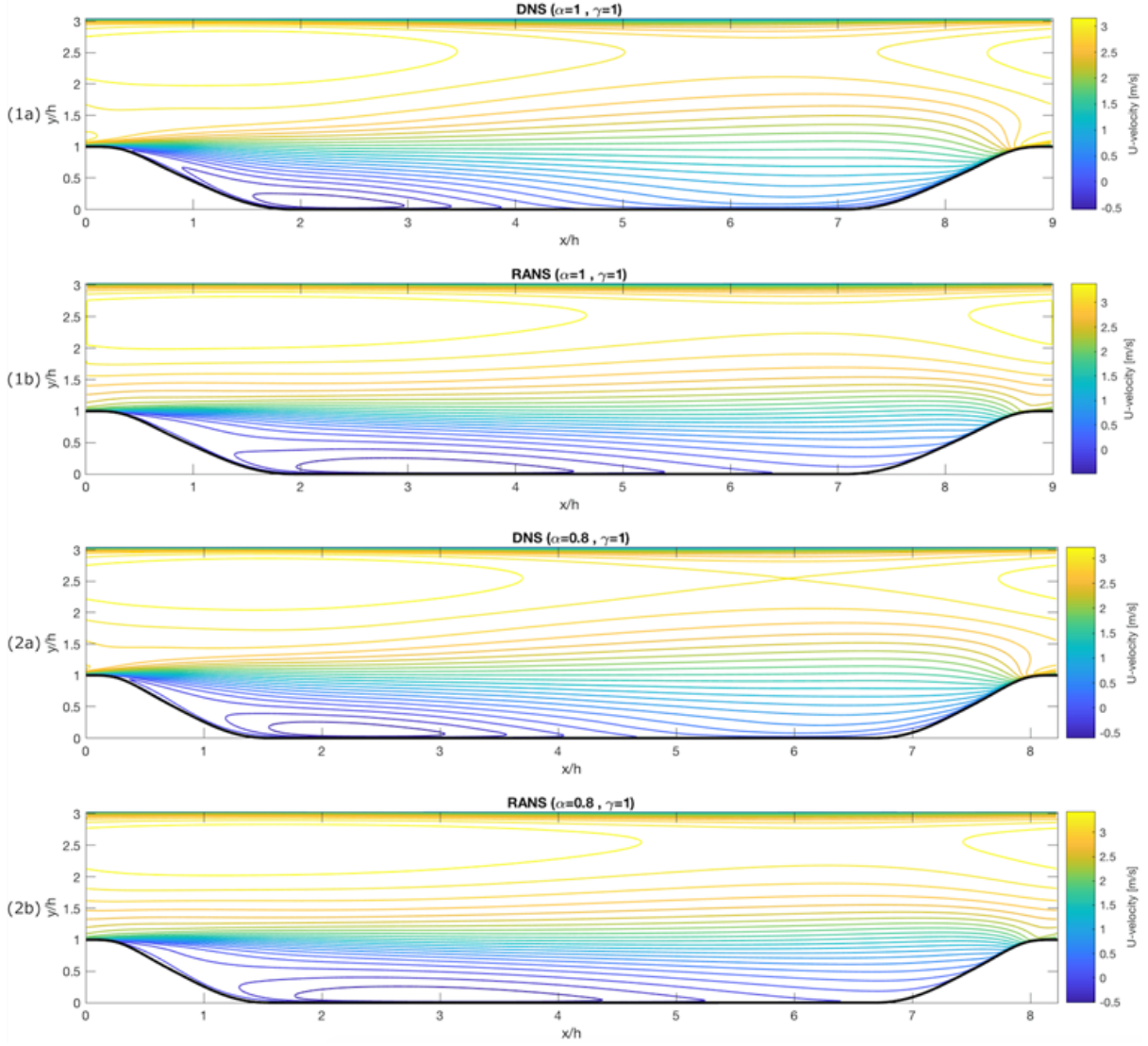


Figure 8: Comparison of horizontal velocity contours of DNS (1a) and RANS (1b) simulation of the reference test case $\alpha = 1, \gamma = 1$ and of DNS (2a) and RANS (2b) simulation of the test case with $\alpha = 0.8, \gamma = 1$.

The correlation coefficient R^2 and the mean absolute relative error ($|M|_{rel}$) are two measures to relate the results of the DNS and RANS simulations (Palar, Tsuchiya and Parks [50]). The definition of these quantities is given in Eq. 30 and Eq. 31 respectively. The function values of the data points are indicated with $f_i^{[data\ set]}$; the mean of all function values of the data set is indicated with $\mu^{[data\ set]}$. Two comments have to be made with respect to the data sets. Firstly, it is assumed that the high-fidelity DNS and low-fidelity RANS data sets are nested. Secondly, the values that are used for the low-fidelity data set are only those where the high-fidelity data points are available (i.e. $N_{hf} = 7$). The values of R^2

and $|M|_{rel}$ are calculated for all QoI listed in section 2.4. The results are summarised in Table 3.

$$R^2 = \frac{\left[\sum_{i=1}^{N_{hf}} \left(f_i^{[DNS]} - \mu^{[DNS]} \right) \left(f_i^{[RANS]} - \mu^{[RANS]} \right) \right]^2}{\sum_{i=1}^{N_{hf}} \left(f_i^{[DNS]} - \mu^{[DNS]} \right)^2 \sum_{i=1}^{N_{hf}} \left(f_i^{[RANS]} - \mu^{[RANS]} \right)^2} \quad (30)$$

$$|M|_{rel} = \frac{1}{N_{hf}} \sum_{i=1}^{N_{hf}} \frac{\left| f_i^{[DNS]} - f_i^{[RANS]} \right|}{\mu^{[DNS]}} \quad (31)$$

Table 3: Correlation (R^2) and mean absolute relative error ($|M|_{rel}$) of DNS and RANS simulations for quantities of interest describing the separation bubble.

Quantity of Interest	R^2	$ M _{rel}$
Height of the bubble at $x/h = 2$	0.7039	0.1629
Height of the bubble at $x/h = 4$	0.0399	2.1384
Bubble length	0.7047	1.2948

In Table 3, the very low correlation and relatively large $|M|_{rel}$ for the height of the separation bubble at $x/h = 4$ are noticed. The RANS model is not able to describe this QoI accurately. The high-fidelity DNS model reattaches generally around this streamwise position, unlike the low-fidelity RANS model as can be seen in Figure 8. For the height of the separation bubble at $x/h = 2$, the correlation between RANS and DNS is relatively large, as for the length of the separation bubble. The large correlation coefficient combined with a rather large $|M|_{rel}$ for the length of the separation bubble forms an opportunity for the hybrid method. The proper trend of the RANS simulations (indicated by the correlation coefficient) will be corrected by the accuracy of the high-fidelity DNS.

4.3. Comparison of the probability distributions of the quantities of interest

The PDFs of the linearly interpolated DNS and RANS models are given for the list of QoI in the left two columns of Figure 12. They illustrate the difference between the DNS and RANS models and show the effect of turbulence models.

By generating a PDF from the linearly interpolated DNS response surface, the true DNS distribution can only be approximated. To obtain the true high-fidelity DNS distribution, an immense amount of DNS would have to be run, which is computationally intractable. This also means that the CPU gain of the hybrid methods cannot be approximated.

The PDF of the DNS response surface contains physically more accurate information since it only uses high-fidelity simulations which are closer to the real physics than the low-fidelity RANS simulations. However, since significantly more low-fidelity RANS points are available, i.e. in this case 30 instead of 7, one can see that statistically the RANS PDF will be better. Moreover, the low-fidelity simulations RANS are available over a larger domain in the $(\alpha - \gamma)$ -space compared to the high-fidelity DNS. Both data sets have specific advantage; computationally expensive data is physically more accurate, a lot of

computationally cheap data over a wider range has a statistical advantage. The goal of the hybrid PDF is to merge the advantages of both types of data sets. The advantage of the DNS -the physical accuracy- and the advantage of the RANS simulations -the stochastic accuracy- will be combined in the hybrid UQ approach, described in Section 5.4.

5. Hybrid modelling combining DNS and RANS

The application of the hybrid methods of Section 3 is described in this section. The test case of the flow over periodically arranged hills has 2 random variables, namely α and γ . A set of $N_{DNS} = 7$ high-fidelity DNS and $N_{RANS} = 30$ low-fidelity RANS simulations is used to test the methods. It has to be stressed that the number of high-fidelity and low-fidelity simulations is only chosen to maintain a reasonable computational cost for this work. The main point of this work is to combine both DNS and RANS simulations in a hybrid framework for UQ to improve the PDF with both physical and statistical accuracy. Also it has to be noted that the pure DNS PDF cannot be computed since it is computationally too expensive. Therefore comparing the hybrid PDF with the pure DNS PDF is also not possible. Moreover, it is also expected that different hybrid methods presented in Section 3 will result in different PDF, since these different methods use different characteristics of the data set. As already stated in Section 3, the IWD method only uses distance as weight factor in the interpolation process unlike the GCK method that uses distance, correlation and regression.

5.1. Application of the hybrid methods to the test case

The hybrid methods that are described in Section 3 are applied to the test case of the flow over the periodically arranged hills. The random variables introducing uncertainty in the geometry are $\xi = [\xi_1, \xi_2] = [\alpha, \gamma]$. The low-fidelity simulations are the RANS simulations ($N_{lf} = N_{RANS} = 30$) and the high-fidelity simulations are the DNS ($N_{hf} = N_{DNS} = 7$). For the IWD-method, the value of the power p in Eq. 7 is selected to be equal to 1, to not assume anything about the curvature of the model in between the available data points.

Both input random variables α and γ are assumed to be normally distributed. To generate the hybrid PDFs, a distribution of the input variables α and γ has to be assumed to execute the Monte Carlo sampling process. In this example both input variables α and γ are normally distributed with mean μ_{input} and standard deviation σ_{input} (namely $\mathcal{N}(\mu_{input}, \sigma_{input}^2)$), as given in Eq. 32. Note that the normal distributions are truncated at the lower and upper bound of each variable, namely $\alpha \in [0.8, 1.2]$ and $\gamma \in [0.5, 1.0]$.

$$\alpha \sim \mathcal{N}(1, 0.25^2) \Big|_{x \in [0.8, 1.2]} \quad \text{and} \quad \gamma \sim \mathcal{N}(0.75, 0.3^2) \Big|_{x \in [0.5, 1.0]} \quad (32)$$

Having normally distributed input random variables means that the Hermite polynomials are used as orthogonal basis functions for the PCE. Using the number of low-fidelity simulations ($N_{RANS} = 30$) and the number of high-fidelity simulations ($N_{DNS} = 7$), the order of the PCE can be determined, bearing

in mind the over-sampling ratio of 2 (Palar, Tsuchiya and Parks [50] and Hosder, Walters and Balch [52]). A summary is given in Table 4. An additive correction PCE is applied as given in Eq. 17. The low-fidelity coefficients c_{lf} are computed using Eq. 15, with vector F being the low-fidelity function values $f_{lf} = f_{RANS}$. The correction coefficients c_C are also computed using Eq. 15, but with vector F being the difference between the low- and high-fidelity function values $f_{hf} - f_{lf} = f_{DNS} - f_{RANS}$. To compute the difference $f_{hf} - f_{lf}$, first a linearly-interpolated response surface of the high-fidelity data points is generated, which subsequently is sampled at the low-fidelity data points.

Table 4: Summary of the variables for the PCER method.

Description	Variable	Value	Variable	Value
Number of simulations	N_{DNS}	7	N_{RANS}	30
Order of the PCE	m_{DNS}	1	m_{DNS}	4
Number of random variables	n	2	n	2
Number of terms in the PCE	N_p	3	N_p	15
Over-sampling ratio	$\frac{N_{eval}}{N_p} = \frac{N_{DNS}}{N_p}$	2.33	$\frac{N_{eval}}{N_p} = \frac{N_{RANS}}{N_p}$	2

For the GCK-method, the CoKriging process is executed using the DACE Matlab toolbox for Kriging. A 0-th order (i.e. polynomial of 0th order) regression function and a Gaussian correlation function are selected. When finding the MLE of the mean, the standard deviation and the hyper-parameters, the lower and upper bound for the genetic algorithm optimization toolbox are set to 10^{-10} and 10 respectively.

5.2. Computational times

The computational time for each DNS was of the order of 24 hours, using 1,024 cores on the UK Supercomputing Facility ARCHER³. The computational time for the RANS simulations was of the order of a couple hours on a powerful workstation. Moreover, the computational time for the hybrid methods was of the order of minutes. This directly proves the applicability of the hybrid methods for uncertainty quantification, where the high-fidelity simulations are computationally expensive, often an order of magnitude higher than their lower-fidelity counterparts.

5.3. Response surfaces

The hybrid response surfaces of the list of QoI generated with the IWD-method and the GCK-method are shown in Figure 9-11. For the PCER-method, the probability distribution is computed directly, without the use of a response surface.

It can be seen that the hybrid surfaces go through the DNS data points and that the surface in between is governed by the RANS data points. Further away from the DNS data points the hybrid surface tends towards the RANS surface, because no high-fidelity data are available. In the regions where the high-fidelity data is not available, i.e. the bottom left and right corner of the (α, γ) -domain, the low-fidelity data helps to generate the hybrid response surface. It has to be noted that the response

³More information on the ARCHER facility can be found here: www.archer.ac.uk

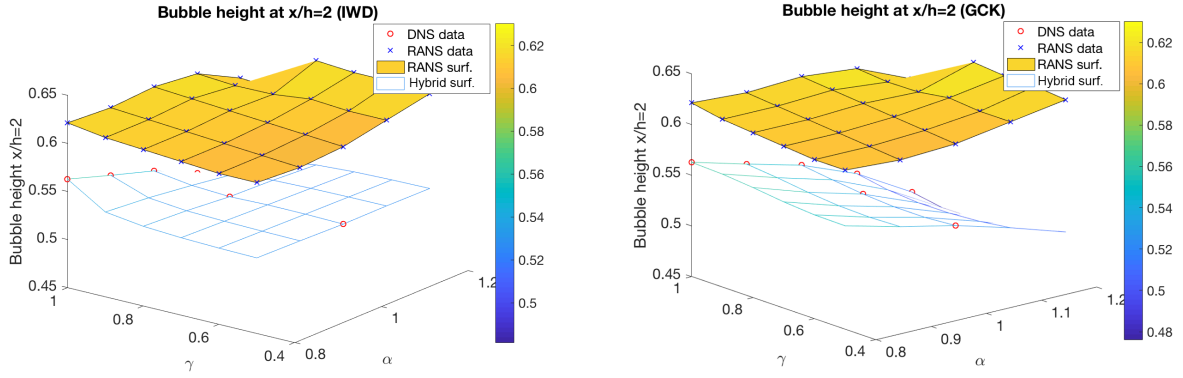


Figure 9: Hybrid response surface for the bubble height at $x/h = 2$ compared to the RANS response surface: Inverse Weighted Distance method (left) and Gaussian CoKriging method (right).

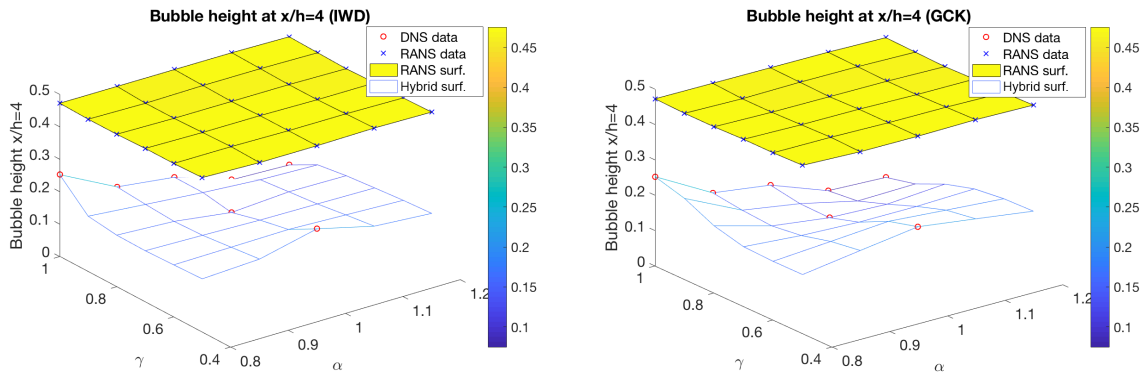


Figure 10: Hybrid response surface for the bubble height at $x/h = 4$ compared to the RANS response surface: Inverse Weighted Distance method (left) and Gaussian CoKriging method (right).

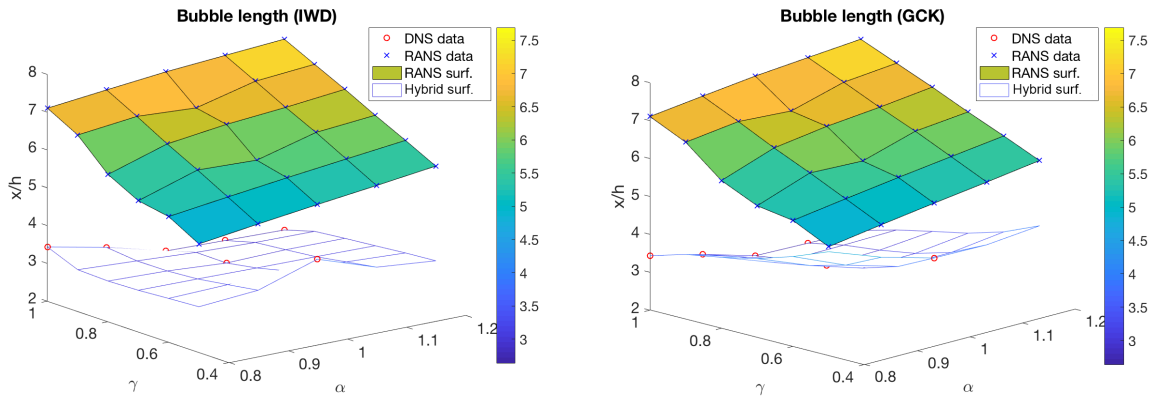


Figure 11: Hybrid response surface for the bubble length compared to the RANS response surface: Inverse Weighted Distance method (left) and Gaussian CoKriging method (right).

surface of linearly interpolated DNS points would not be available outside the domain of the data points, except with extrapolation. In this region the hybrid methods provide a direct advantage by enabling the approximation of the response surface in a wider range.

5.4. Probability distributions

The PDFs of the list of QoI generated with the different hybrid methods of Section 3 are shown in the right 3 columns of Figure 12.

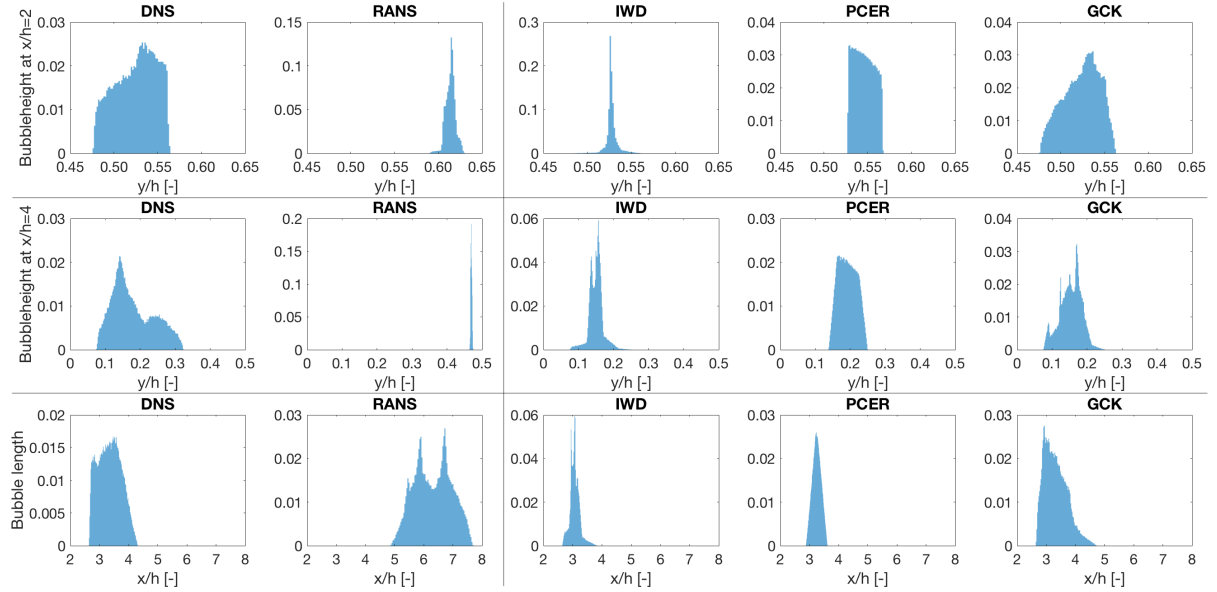


Figure 12: PDF of the output QoI using DNS and RANS results only (left two columns); PDF of the output QoI using the hybrid methods of Section 3: Inverse Weighted Distance (IWD), Polynomial Chaos Expansion with Regression (PCER), Gaussian CoKriging (GCK). The input variables are normally distributed.

The PDFs using purely DNS or purely RANS simulations are already described in Section 4.3. These PDFs are compared to the hybrid PDFs.

Firstly, the conceptual difference between the DNS and RANS model becomes really apparent when comparing the respective mean values for different QoI. These are indicated with red dots in Figure 13. The hybrid methods correct the wrongly predicted RANS mean value towards the mean value of the DNS. Secondly, when comparing the range of the different PDF it can be seen that for the three QoI, the IWD- and GCK-method capture the range of the DNS PDF better compared to the PCER method. Note that the standard deviation of the different distributions is also given in Figure 13 (the green dots indicate $\mu \pm \sigma$). The shape of the PDF and more specifically its deviation from the horizontal symmetry, is given by the skewness parameter. The Fisher-Pearson coefficient of skewness of a data set is given in Eq. 33 where E indicates the expectation of a stochastic variable (Doane and Seward [59]).

$$\beta = \frac{m_3}{(m_2)^{3/2}} \quad \text{where} \quad m_3 = E(x - \mu)^3 \quad \text{and} \quad m_2 = E(x - \mu)^2 \quad (33)$$

The skewness values for the different PDF are also given in Figure 13. For the well-correlated QoI (height of the bubble at $x/h = 2$ and bubble length) the GCK-method predicts a similar skewness. For the bubble height at $x/h = 2$ it is even the only method doing so when looking at the sign and magnitude of β in Figure 13. For the bubble height at $x/h = 4$ the skewness predicted by the three methods deviates

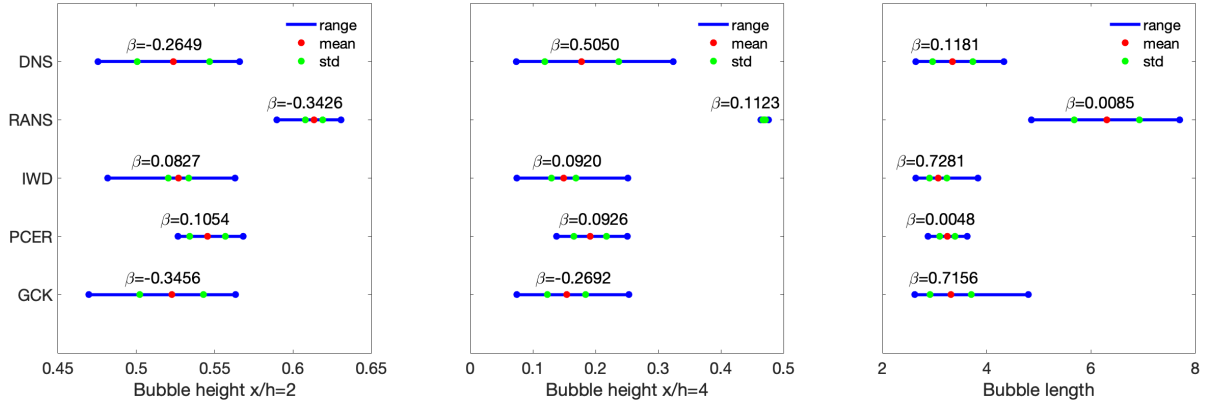


Figure 13: Comparison of the range, mean, standard deviation (std) and skewness (β) of the PDF of DNS, RANS, Gaussian CoKriging (GCK), Inverse Weighted Distance (IWD) and Polynomial Chaos Expansion with Regression (PCER).

considerably from the skewness of the DNS PDF. In general, when comparing the different PDF by visual inspection, one can see the following features. The shape of the PDF of the IWD-method is very similar to the shape of the RANS only PDF, while the shape of the GCK-method PDF is more similar to the DNS only PDF.

Since the pure DNS PDF can never be obtained exactly because of the intractable computational cost, it can only be approximated. The PDF resulting from only using the DNS data points will not give a good approximation because too few data points are available. On the other hand, the PDF resulting from only using the RANS data points will also not be a good approximation because of the RANS model error. Therefore, by using a hybrid data set to compute the output PDF will result in an improvement of the approximation. From the above analysis it can be seen that for the test case of the flow over periodically arranged hills, the GCK-method is the best method.

5.5. Influence of CoKriging correlation model

The influence of the correlation model of the CoKriging method is studied by running the example test case with an exponential correlation model instead of the Gaussian correlation model. The output PDFs can be seen in Figure 14. They are compared to the PDF of the GCK method in the 5th column of Figure 12. From Figure 14 it can be seen that the Exponential CoKriging (ECK) method also tends more towards the PDF of the pure DNS model. This is similar to the PDF of the GCK method. This means that the favourable property of capturing the pure DNS PDF is conserved by varying the correlation model. However, the GCK method still captures the pure DNS shape better.

5.6. Influence of input probability distribution

The example test case is also run for a uniform input distribution instead of the previously used normal distribution. The output PDF can be seen in Figure 15.

The PDF are compared to the PDF in the 5th column of Figure 12. The output PDF of the uniform distribution are generally more flat, which resembles the shape of the uniform distribution itself. This is

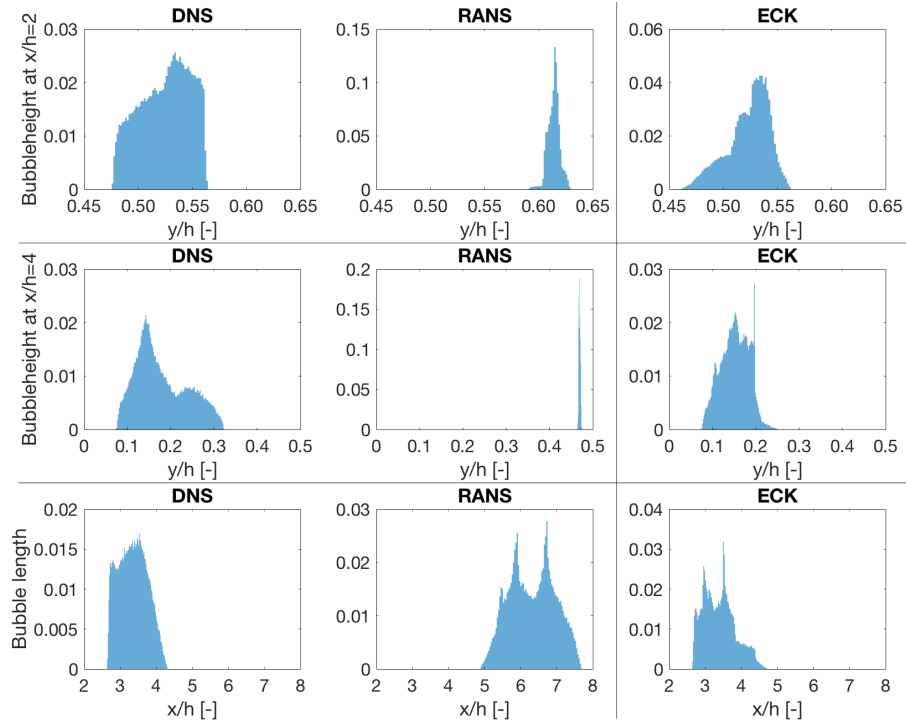


Figure 14: PDF of the output QoI using DNS and RANS results only (left two columns); PDF of the output QoI using the hybrid Exponential CoKriging (ECK). The input variables are normally distributed.

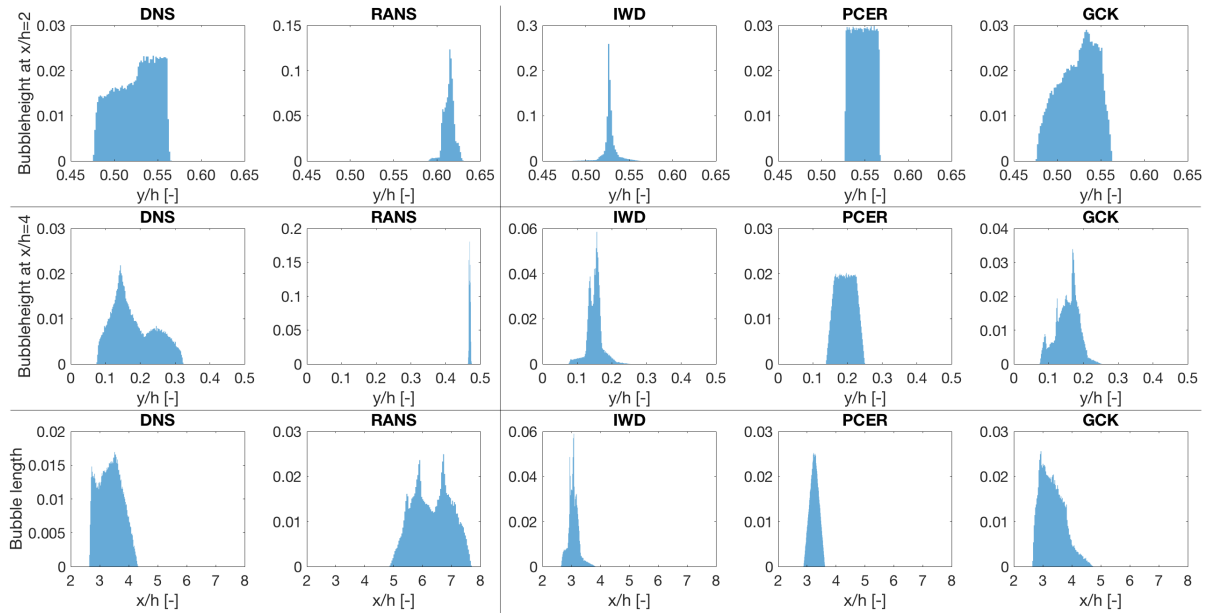


Figure 15: PDF of the output QoI using DNS and RANS results only (left two columns); PDF of the output QoI using the hybrid methods of Section 3: Inverse Weighted Distance (IWD), Polynomial Chaos Expansion with Regression (PCER), Gaussian CoKriging (GCK). The influence of the input distribution is studied by selecting a uniform input distribution.

really apparent in the PCER-method, which uses the orthogonal polynomials corresponding to specific input distribution (i.e. the uniform distribution) to generate the PCE.

6. Conclusions

In this work, the possibility of using non-intrusive multi-fidelity methods combining both RANS simulations and DNS for uncertainty quantification (UQ) is examined. The methods are applied on a flow over 2D periodically arranged hills with uncertainty introduced in the hill steepness angle and subsequent hill separation. As the RANS model is known to struggle with separation from curved surfaces and with reattachment, the test case is well-suited to perform an example multi-fidelity UQ study. Three different multi-fidelity methods are tested, namely an inverse weighted-distance method, a polynomial chaos expansion method using weighted regression, and a Gaussian CoKriging method. The main objective of all these hybrid methods is to combine both low-fidelity RANS simulations and high-fidelity DNS in a multi-fidelity framework to be able to make more accurate computations when performing UQ. When analyzing the application of the methods to the flow test case, the three methods all correct the mean of the probability distribution function (PDF) obtained using purely RANS simulations towards the mean of the PDF using purely DNS. However, the CoKriging method and in particular the Gaussian CoKriging method is found to perform better when other shape parameters of the PDF such as range and skewness are compared. Therefore the Gaussian CoKriging method is considered as the best multi-fidelity method compared to the other methods suggested in this study. It has to be noted that for poorly correlated quantities of interest, UQ using the multi-fidelity approaches is challenging. One of the main advantages of the hybrid methods is that they allow for a more efficient framework for UQ when data sets with different levels of fidelity are available. Instead of having to run high-fidelity data over the entire range of the domain, the computational cost can be reduced by making use of the low-fidelity data points. Further research into the effects of different correlation models of the CoKriging method or the effect of different input probability distributions on the multi-fidelity PDFs is encouraged. It is also recommended to study which properties of the low- and high-fidelity data will result in a high-quality multi-fidelity model. The effectiveness of the different hybrid methods will be discussed in a future study.

7. Acknowledgements

The authors acknowledge the use of computational resources from the Certainty cluster awarded by the National Science Foundation to Stanford Center of Turbulence Research. Sylvain Laizet acknowledges the EPSRC UK Turbulence Consortium (Research grant EP/L000261/1) for access to UK supercomputing resources. Laurens Voet would like to acknowledge Kanika Gakhar for her helpful suggestions throughout the review process.

Conflict of Interest

The authors declare that they have no conflict of interest.

References

- [1] N. Thakur, A. Keane, P. B. Nair, Probabilistic analysis of manufacturing uncertainty in turbine blades, in: International Design Engineering Technical Conferences and Computers and Information in Engineering Conference, Vol. 49026, 2009, pp. 1057–1066.
- [2] A. Abolfathi, D. J. O’Boy, S. J. Walsh, A. M. Dowsett, S. A. Fisher, The uncertainty in stiffness and damping of an automotive vehicle’s trim-structure mounts and its effect on the variability of the vibration transfer function, Proceedings of the Institution of Mechanical Engineers, Part C: Journal of Mechanical Engineering Science 232 (15) (2018) pp. 2587–2598.
- [3] S. Amaral, E. de la Rosa Blanco, D. Allaire, K. E. Willcox, Uncertainty Quantification of Aviation Fuel Burn Performance A PARTNER Project 48 report Uncertainty Quantification of Aviation Fuel Burn Performance A PARTNER Project 48 Report, 2016.
- [4] A. Loeven, H. Bijl, Airfoil analysis with uncertain geometry using the probabilistic collocation method, in: 49th AIAA/ASME/ASCE/AHS/ASC Structures, Structural Dynamics, and Materials Conference, 16th AIAA/ASME/AHS Adaptive Structures Conference, 10th AIAA Non-Deterministic Approaches Conference, 9th AIAA Gossamer Spacecraft Forum, 4th AIAA Multidisciplinary Design Optimization Specialists Conference, 2008, p. 2070.
- [5] R. Schnell, G. Ashcroft, L. Hoehe, Geometric variability and its influence on steady and unsteady fan aerodynamic performance, in: Proceeding of the 29th International Congress of Aeronautical Sciences, 2014, pp. 2014–0105.
- [6] F. Montomoli, M. Massini, S. Salvadori, F. Martelli, Geometrical Uncertainty and Film Cooling: Fillet Radii, in: Vol. 4 Heat Transf. Parts A B, 2010.
- [7] A. Panizza, R. Valente, D. Rubino, L. Tapinassi, Impact of manufacturing variability on the aerodynamic performance of a centrifugal compressor stage with curvilinear blades, in: Proc. ASME Turbo Expo, 2016.
- [8] S. Chan, A. H. Elsheikh, A machine learning approach for efficient uncertainty quantification using multiscale methods, Journal of Computational Physics 354 (2018) pp. 493–511.
- [9] A. Cunha Jr, R. Nasser, R. Sampaio, H. Lopes, K. Breitman, Uncertainty quantification through the Monte Carlo method in a cloud computing setting, Comput. Phys. Commun. 185 (5) (2014) pp. 1355–1363.
- [10] A. O’Hagan, Polynomial chaos: A tutorial and critique from a statistician’s perspective, SIAM/ASA J. Uncertainty Quantification 20 (2013) pp. 1–20.
- [11] M. Köppel, I. Kröker, C. Rohde, Intrusive uncertainty quantification for hyperbolic-elliptic systems governing two-phase flow in heterogeneous porous media, Computational Geosciences 21 (4) (2017) pp. 807–832.
- [12] R. Ahlfeld, F. Montomoli, A Single Formulation for Uncertainty Propagation in Turbomachinery:

- SAMBA PC, J. Turbomach., 2017.
- [13] E. A. Dow, Q. Wang, The Implications of Tolerance Optimization on Compressor Blade Design, *Journal of Turbomachinery* 137 (10), 2015.
 - [14] A. Doostan, G. Geraci, G. Iaccarino, A bi-fidelity approach for uncertainty quantification of heat transfer in a rectangular ribbed channel, in: *ASME Turbo Expo 2016: Turbomachinery Technical Conference and Exposition*, American Society of Mechanical Engineers Digital Collection, 2016.
 - [15] C. D. Argyropoulos, N. C. Markatos, Recent advances on the numerical modelling of turbulent flows, *Applied Mathematical Modelling* 39 (2) (2015) pp. 693–732.
 - [16] P. Moin, K. Mahesh, Direct numerical simulation: a tool in turbulence research, *Annual review of fluid mechanics* 30 (1) (1998) pp. 539–578.
 - [17] G. N. Coleman, R. D. Sandberg, A primer on direct numerical simulation of turbulence - methods, procedures and guidelines, University of Southampton, Technical Report No. AFM-09/01a, 2010.
 - [18] L. Prandtl, Bericht über untersuchungen zur ausgebildeten turbulenz, *Zeitschrift für Angewandte Mathematik und Mechanik (ZAMM-Journal of Applied Mathematics and Mechanics)* 5 (2) (1925) pp. 136–139.
 - [19] P. Spalart, S. Allmaras, A one-equation turbulence model for aerodynamic flows, in: *30th aerospace sciences meeting and exhibit*, 1992, p. 439.
 - [20] D. C. Wilcox, *Formulation of the k- ω Turbulence Model Revisited*, AIAA J., 2008.
 - [21] P. Sagaut, *Large eddy simulation for incompressible flows: an introduction*, Springer Science & Business Media, 2006.
 - [22] K. Duraisamy, G. Iaccarino, H. Xiao, Turbulence modeling in the age of data, *Annual Review of Fluid Mechanics* 51 (2019) pp. 357–377.
 - [23] J.-X. Wang, J.-L. Wu, H. Xiao, Physics-informed machine learning approach for reconstructing reynolds stress modeling discrepancies based on dns data, *Physical Review Fluids* 2 (3) (2017) p. 034603.
 - [24] J.-L. Wu, H. Xiao, E. Paterson, Physics-informed machine learning approach for augmenting turbulence models: A comprehensive framework, *Physical Review Fluids* 3 (7) (2018) p. 074602.
 - [25] A. Vollant, G. Balarac, C. Corre, Subgrid-scale scalar flux modelling based on optimal estimation theory and machine-learning procedures, *Journal of Turbulence* 18 (9) (2017) pp. 854–878.
 - [26] M. Gamahara, Y. Hattori, Searching for turbulence models by artificial neural network, *Physical Review Fluids* 2 (5) (2017) p. 054604.
 - [27] B. E. Launder, B. Sharma, Application of the energy-dissipation model of turbulence to the calculation of flow near a spinning disc, *Letters in heat and mass transfer* 1 (2) (1974) pp. 131–137.
 - [28] F. Menter, M. Kuntz, R. Langtry, Ten years of industrial experience with the sst turbulence model, *Turbul. Heat Mass Transf.*, 2003 4.

- [29] S. B. Pope, Turbulent flows (2001).
- [30] J.-X. Wang, R. Sun, H. Xiao, Quantification of uncertainties in turbulence modeling: A comparison of physics-based and random matrix theoretic approaches, *International Journal of Heat and Fluid Flow* 62 (2016) pp. 577–592.
- [31] H. Raiesi, U. Piomelli, A. Pollard, Evaluation of Turbulence Models Using Direct Numerical and Large-Eddy Simulation Data, *J. Fluids Eng.*, 2011.
- [32] H. N. Najm, Uncertainty quantification and polynomial chaos techniques in computational fluid dynamics, *Annual review of fluid mechanics* 41 (2009) pp. 35–52.
- [33] S. Salehi, M. Raisee, M. J. Cervantes, A. Nourbakhsh, An efficient multifidelity l1-minimization method for sparse polynomial chaos, *Comput. Methods Appl. Mech. Eng.*, 2018.
- [34] M. Breuer, N. Peller, C. Rapp, M. Manhart, Flow over periodic hills - Numerical and experimental study in a wide range of Reynolds numbers, *Comput. Fluids*, 2009.
- [35] M. Marquillie, J.-P. Laval, R. Dolganov, Direct numerical simulation of a separated channel flow with a smooth profile, *Journal of Turbulence* (9) (2008) N1.
- [36] M. S. Gritskevich, A. V. Garbaruk, J. Schütze, F. R. Menter, Development of DDES and IDDES formulations for the $k-\omega$ shear stress transport model, *Flow, Turbul. Combust.*, 2012.
- [37] C. P. Mellen, J. Frohlich, W. Rodi, Large Eddy Simulation of the flow over periodic hills: Introduction and Test Case Geometry, 16th IMACS world Congr., 2000.
- [38] A. Huminic, G. Huminic, Aerodynamic study of a generic car model with wheels and underbody diffuser, *International Journal of Automotive Technology* 18 (3) (2017) pp. 397–404.
- [39] H. H. Choi, V. T. Nguyen, J. Nguyen, Numerical Investigation of Backward Facing Step Flow over Various Step Angles, in: *Procedia Eng.*, 2016.
- [40] H. Xiao, J.-L. Wu, J.-X. Wang, R. Sun, C. Roy, Quantifying and reducing model-form uncertainties in reynolds-averaged navier–stokes simulations: A data-driven, physics-informed bayesian approach, *Journal of Computational Physics* 324 (2016) 115–136.
- [41] G. P. Almeida, D. F. Durão, M. V. Heitor, Wake flows behind two-dimensional model hills, *Exp. Therm. Fluid Sci.*, 1993.
- [42] M. Quadrio, B. Frohnafel, Y. Hasegawa, Does the choice of the forcing term affect flow statistics in dns of turbulent channel flow?, *European Journal of Mechanics-B/Fluids* 55 (2016) 286–293.
- [43] S. Laizet, E. Lamballais, High-order compact schemes for incompressible flows: A simple and efficient method with quasi-spectral accuracy, *Journal of Computational Physics* 228 (16) (2009) pp. 5989–6015.
- [44] S. Laizet, N. Li, Incompact3d: A powerful tool to tackle turbulence problems with up to $0 (10^5)$ computational cores, *International Journal for Numerical Methods in Fluids* 67 (11) (2011) 1735–1757.

- [45] H. Xiao, J.-L. Wu, S. Laizet, L. Duan, Flows over periodic hills of parameterized geometries: A dataset for data-driven turbulence modeling from direct simulations, *Computers & Fluids* (2020) p. 104431.
- [46] S. K. Lele, Compact finite difference schemes with spectral-like resolution, *Journal of computational physics* 103 (1) (1992) pp. 16–42.
- [47] V. E. Garzon, D. L. Darmofal, Impact of geometric variability on axial compressor performance, *J. Turbomach.* 125 (4) (2003) pp. 692–703.
- [48] D. Shepard, A two-dimensional interpolation function for irregularly-spaced data, in: *Proc. 1968 23rd ACM Natl. Conf.*, 1968.
- [49] R. Ahlfeld, B. Belkouchi, F. Montomoli, SAMBA: Sparse Approximation of Moment-Based Arbitrary Polynomial Chaos, *J. Comput. Phys.*, 2016.
- [50] P. S. Palar, T. Tsuchiya, G. T. Parks, Multi-fidelity non-intrusive polynomial chaos based on regression, *Comput. Methods Appl. Mech. Eng.*, 2016.
- [51] S. Hosder, R. Walters, Non-Intrusive Polynomial Chaos Methods for Uncertainty Quantification in Fluid Dynamics, in: *48th AIAA Aerosp. Sci. Meet. Incl. New Horizons Forum Aerosp. Expo.*, 2010.
- [52] S. Hosder, R. Walters, M. Balch, Efficient Sampling for Non-Intrusive Polynomial Chaos Applications with Multiple Uncertain Input Variables, in: *48th AIAA/ASME/ASCE/AHS/ASC Struct. Struct. Dyn. Mater. Conf.*, 2007.
- [53] L. W.-T. Ng, M. Eldred, Multifidelity Uncertainty Quantification Using Non-Intrusive Polynomial Chaos and Stochastic Collocation, in: *53rd AIAA/ASME/ASCE/AHS/ASC Struct. Struct. Dyn. Mater. Conf. AIAA/ASME/AHS Adapt. Struct. Conf. AIAA*, 2012.
- [54] D. G. Krige, A statistical approach to some basic mine valuation problems on the Witwatersrand (1952).
- [55] A. I. Forrester, A. Sóbester, A. J. Keane, Multi-fidelity optimization via surrogate modelling, *Proc. R. Soc. A Math. Phys. Eng. Sci.*, 2007.
- [56] S. N. Lophaven, H. B. Nielsen, J. Sondergaard, A. Dace, A matlab kriging toolbox, Technical University of Denmark, Kongens Lyngby, Technical Report No. IMMTR-2002 12, 2002.
- [57] L. Klaus, S. Eichstädt, Monte-carlo-based uncertainty propagation with hierarchical models—a case study in dynamic torque, *Metrologia* 55 (2) (2018) S70.
- [58] T. Bartel, S. Stoudt, A. Possolo, Force calibration using errors-in-variables regression and monte carlo uncertainty evaluation, *Metrologia* 53 (3) (2016) 965.
- [59] D. P. Doane, L. E. Seward, Measuring skewness: a forgotten statistic?, *Journal of statistics education* 19 (2), 2011.